# Mapping Deformation Over Greater Houston Using InSAR

**Prepared for:**

**Harris-Galveston Subsidence District**
1660 W Bay Area Blvd.
Friendswood, TX 77546
(281) 486-1105

**Fort Bend Subsidence District**
301 Jackson Street, Suite 639
Richmond, TX 77469
(281) 342-3273

**Prepared by:**

**Dr. Feifei Qu and Dr. Zhong Lu**
Dedman College of Humanities and Sciences, Southern Methodist University
P.O. Box 750235
Dallas, TX 75275
(214) 768-0101

**October 2022**

# TABLE OF CONTENTS

# LIST OF TABLES



# LIST OF FIGURES

# ABBREVIATIONS AND ACRONYMS

| | |
|---|---|
| ALOS-1 | Advanced Land Observing Satellite-1 |
| ALOS-2 | Advanced Land Observing Satellite-2 |
| ASAR | advanced synthetic aperture radar |
| CORS | continuously operating reference station |
| CSK | Cosmo-SkyMed |
| DEM | digital elevation model |
| Envisat | environmental satellite |
| ERS | European Remote Sensing |
| ESA | European Space Agency |
| FBSD | Fort Bend Subsidence District |
| GH | greater Houston |
| GPS | global positioning system |
| HGSD | Harris-Galveston Subsidence District |
| InSAR | interferometric synethic aperture radar |
| ISA | Italian Space Agency |
| JAXA | Japan Aerospace Exploration Agency |
| LiDAR | light detection and ranging |
| LOS | line of sight |
| MTI | multi-temporal InSAR |
| NASA | National Aeronautics and Space Administration |
| NGS | National Geodetic Survey |
| PALSAR | phased array type L-band synthetic aperture radar |
| PAM | periodically measured |
| PS | persistent scatterers |
| RMSE | root means square error |
| SAR | synethic aperature radar |
| SBAS | small baseline subset |
| SFP | slowly-varying filtered phase |
| SRTM | shuttle radar topography mission |
| TRAIN | toolbox for reducing atmospheric InSAR noise |
| US | United States |
| UTM | universal traverse mercator |

# Executive Summary

Land subsidence in Greater Houston (GH) region can cause damage to buildings and infrastructures that may lead to substantial loss of wetland habitat and more frequent flooding. This project investigates land surface deformation by using Multi-Temporal Interferometric Synthetic Aperture Radar (InSAR) (MTI) technique that mitigates inherent artifacts caused by the atmosphere and maximizes the density and reliability of the measured deformation of the land surface. This project uses the MTI technique to analyze the evolution of the deformation of the land surface across the GH.

We have constructed average deformation maps from 1993 through 2020 over GH using radar imagery from ERS, ALOS-1, Envisat, Cosmo-SkyMed, ALSO-2 and Sentinel 1A/B satellites. Using global positioning systems (GPS) and extensometer observations, we report that the accuracy of our InSAR measurements of long-term subsidence can reach 2-11 millimeters per year (mm/yr). Subsidence rates in the northwest decreased from around 53 mm/yr in the 1990s to about 30mm/yr from 2005 to 2011 after the reduction in groundwater withdrawal implemented in Harris and Fort Bend Counties. The areas of maximum subsidence transferred from Spring and The Woodlands to Katy starting in 2016. From 2016 to 2020, GH can generally be characterized as subsidence in the northwest and uplift in the southeast.

Besides the regional deformation patterns, localized features of subsidence and uplift can be spotted at some locations from 1992 to 2020. Four (4) major subsidence features were analyzed in greater detail at Stratton Ridge oil field, Mont Belvieu, Seabrook, and Channelview using results from ERS, ALOS-1, Envisat, ALSO-2 and Sentinel 1A/B. These locations show a long-term and high-rate subsidence feature, which is likely due to hydrocarbon-related activities or ongoing differential movement of salt domes. InSAR observations have also recognized localized and transient uplift features that occur over gas storage facilities surrounded by regional subsidence.

InSAR results have enabled the identification of fault lines across the GH region. InSAR mapped faults were recognized from the steep phase discontinuities caused by the differential movement of two (2) fault blocks from InSAR-derived velocity maps. Three (3) broad-scale active faulting zones were imaged over the northern GH region: the Hockley fault System, the Big Barn fault System and the Conroe Fault System.

Land subsidence over the GH is not solely attributed to a single component. The subsidence mechanisms include the combined effects of groundwater extraction, tectonic process, salt dome activity, and hydrocarbon extraction. The combination of multiple datasets from analyzing the land surface with InSAR to GPS data as well as aquifer data from extensometers and water-levels aid in the identification of subsidence mechanisms in GH. Additionally, the depressurization of petroleum reservoirs and salt dome dynamics are other subsidence mechanisms that may impact the GH region. Overall, aquifer compaction related to groundwater withdrawal is the primary cause on observed regional subsidence over GH. The correlation between the groundwater level change and the InSAR annual deformation rate is high, with a correlation value of about 0.8. Our deformation mapping can help better understand land deformation rates and extents, identify the processes responsible for the observed deformation, and provide a critical dataset for hazard prediction and mitigation.

# 1.0 Background

Subsidence is a nationwide problem with approximately 44,000 $km^2$ in 45 states within the United States (US) that have permanently subsided (Galloway, 2008). Land subsidence is the sinking of the land surface and has significant impacts. Land subsidence can cause increased flooding, extensive damages to infrastructure from buildings to roadways, and reactivation of faults that generate surficial fissures. The loss of elevation and change in topographic gradients can worsen flooding, leading to the permanent submergence and more frequent flooding in the coastal regions (Coplin and Galloway, 1999; Morton, 2003). In addition, the Greater Houston (hereinafter GH) region experienced socioeconomic devastation caused by the unprecedented flooding after Hurricane Harvey on August 25, 2017. Therefore, constant and accurate measurements of the land surface are crucial to better understand deformation mechanisms and provide insight on how to effectively manage resources to prevent land subsidence.

GH region, comprising Harris, Galveston, Fort Bend, Montgomery, Brazoria, Liberty, San Jacinto, Walker, Grimes, Waller and Chambers counties, has been negatively affected by land surface deformation, especially subsidence, for decades. GH is the largest metropolitan region in US that was affected by land subsidence because of the widespread hydrocarbon production and groundwater pumping (Holzer and Galloway, 2005). Land-surface subsidence caused by fluid withdrawals was first documented in the Baytown area in conjunction with the Goose Creek oil field in southeastern Harris County (Pratt and Johnson, 1926). Approximately 8,300 $km^2$ of land in the GH area had subsided more than 30 centimeters by 1979 (Coplin and Galloway, 1999). Subsidence continued throughout the 20th century as a result of groundwater withdrawal that depressurized the major aquifers in this area, thus resulting in the compaction of clay layers of the aquifer sediments (Kasmarek et al., 2010).

Located in the southeastern part of Texas along the Gulf Coast, GH is composed of thousands of meters of Cenozoic sedimentary deposits that form the Gulf Coast Aquifer (Baker Jr, 1979). The Gulf Coast Aquifer extends from Florida to Mexico along the coastal part of the Gulf of Mexico and about 1 million acre-feet (3.258 trillion gallons) per year of groundwater was withdrawn from this aquifer system during the early-to-mid 20th century (Ashworth, 1995; Robert E. Mace et al., 2006). The Gulf Coast Aquifer consists of interbedded gravels, sands, clays, and silts of Oligocene age and younger (Martin and Whiteman, 1999). The Tertiary and Quaternary sedimentary beds dip and thicken southeast toward the Gulf of Mexico and are divided into five (5) hydrogeologic units: the Chicot aquifer, the Evangeline aquifer, the Burkeville confining unit, the Jasper aquifer, and the Catahoula confining unit from youngest to oldest (Baker Jr, 1979, 1986).

The complex geologic setting, laterally diverse hydrogeologic units, regional faults, and salt dome movement in GH region (Coplin and Galloway, 1999) have made it difficult to monitor and characterize the cause of land subsidence. Starting in the early 1990s, the Harris-Galveston Subsidence District (HGSD) and National Geodetic Survey (NGS) conducted first-order leveling surveys using a combination of global positioning systems (GPS) survey campaign and periodically measured (PAM) surveys to measure subtle

height changes to the land surface elevation (Bawden et al., 2012; Kasmarek et al., 2010; Kasmarek et al., 2012; Kearns et al., 2018; Wang and Soler, 2013; Wang et al., 2017; Wang et al., 2015; Wang et al., 2014; Wang et al., 2013; Yu et al., 2014). Even though ground-based monitoring techniques and the GPS measurements provide high-accuracy land surface deformation measurements at distinct locations, they have limitations in providing more regional and comprehensive information on land surface deformation. Because the heavy consumption of groundwater under the spatially-variant hydrogeology of the Gulf Coast aquifer can induce significant subsidence, temporally and spatially dense observations are required to understand the complicated characteristics underlying the land surface deformation.

Interferometric Synthetic Aperture Radar (InSAR) has demonstrated its capability to measure regional or local land surface deformation caused by land subsidence, landslides, earthquakes, and volcanoes among others (Lu and Danskin, 2001; Lu and Dzurisin, 2014; Massonnet et al., 1993; Wright et al., 2001; Wright et al., 2004). In contrast to the ground-based measurements, the satellite InSAR technique has the ability to measure deformation with a centimeter- to millimeter-level precision over a large area. The conventional InSAR method was applied to investigate land surface subsidence based on individual interferograms (Amelung et al., 1999; Bawden et al., 2001; Lu and Danskin, 2001). However, the spatial and temporal decorrelation between SAR acquisitions often restricts robust measurement and thereby the retrieval of reliable land surface deformation from the conventional InSAR method (Zebker and Villasenor, 1992). In addition, the accuracy of the InSAR measurements can be significantly reduced by the errors in satellite orbit determination and atmospheric artifacts (Fattahi and Amelung, 2016; Ferretti et al., 2001). Accordingly, the Multi-Temporal InSAR (MTI) techniques, such as Persistent Scatterers InSAR (PSInSAR), Small Baseline Subset (SBAS) InSAR, and SqueeSAR, have been developed to map land surface deformation by overcoming the temporal/spatial decorrelation and minimizing the artifacts existing in the conventional InSAR (Bekaert et al., 2015; Ferretti et al., 2011; Ferretti et al., 2001; Hooper et al., 2004; Mora et al., 2003). The MTI technique has facilitated land subsidence monitoring in many urban areas and coastal areas (Buckley et al., 2003; Cigna et al., 2012; Fruneau and Sarti, 2000; Kim et al., 2015; Kim et al., 2005; Qu et al., 2014), such as Santa Clara valley aquifer, located in the San Francisco Bay Area, which has experienced a long history of land subsidence resulting from the excessive pumping of groundwater (Chaussard et al., 2014; Schmidt and Bürgmann, 2003).

Conventional InSAR processing and its applications over the GH face three (3) main challenges: tropospheric artifacts, ionospheric anomalies, and decorrelation over non-urban areas. First, tropospheric delays due to water vapors can amount up to 10 cm in LOS (line-of-sight) range change for a single interferogram (Lu and Dzurisin, 2014), and even more remarkable over the coastal area with a larger amount of water vapors. Second, for L-band SAR images such as ALOS-1/ALOS-2, ionospheric anomalies can reach 11.8 cm across ALOS-1 azimuth extent (Fattahi, 2017). Third, the shorter wavelength (such as C-band) data are likely to decorrelate due to the vegetation interferences. The conventional InSAR has been applied in GH region (Stork & Sneed, 2002; Buckley et al., 2003; Bawden et al., 2012; Khan et al., 2014). The above literatures identified land subsidence stages in 1992 through 2002 by the analysis of

individual interferograms based on the conventional InSAR method, where artifacts caused by variations in atmospheric conditions and errors in satellite orbit were not optimally mitigated.

This project aims at providing a comprehensive analysis on the temporal and spatial land surface deformation in GH using an improved MTI technique. Through combining both PSInSAR and SBAS techniques, MTI can increase the spatial density of usable signal, allowing the identification of persistent scatterers (PSs) that dominate the scattering from the resolution element and slowly-varying filtered phase (SFP) pixels whose phases, when filtered, decorrelate little over short time intervals (Hooper, 2008; Qu et al., 2015; Qu et al., 2014). All of the available SAR images, including ERS, Envisat, Sentinal-1, ALOS-1, ALOS-2, and Cosmo-SkyMed SAR images, have been used to: 1) unravel the characteristics of ground deformation at a finer spatial resolution over the GH from 1992 to 2020, and 2) assess the impact that fluid withdrawal (i.e., groundwater withdrawal and hydrocarbon extraction) have in land surface deformation. We have extracted data from GPS and extensometer measurements to validate and compare with our results from MTI processing. Our MTI-derived subsidence maps have improved our understanding of subsidence rates, their geographic distribution, and temporal variability and mechanisms, and will provide a scientific basis to minimize the undesired geohazards over the GH.

# 2.0 InSAR processing

## 2.1 Methodology

We have utilized MTI to map land surface deformation over the GH. The MTI techniques, which are composed of PSInSAR and SBAS InSAR algorithms, aim at overcoming the limitations in conventional InSAR (Berardino et al., 2002; Ferretti et al., 2001; Hooper, 2008; Hooper et al., 2004). The main idea of MTI is to detect ground targets that remain coherent and utilize spatial and temporal filters to suppress the atmospheric artifacts that plague conventional InSAR products. We have processed SAR data over GH and derived the average land surface deformation rate maps from 1993 to 2020 using the MTI procedures outlined in (Qu et al., 2019; Qu et al., 2015).

## 2.2 SAR Datasets

We have downloaded the complete (archived) ERS, Envisat, ALOS-1 and Sentinel-1A/B imagery acquired from 1993 to 2020. The GH region is covered by a total of 30 ERS scenes from two (2) adjacent descending satellite tracks (1993/1995-1997/2000) acquired by European Space Agency (ESA), 38 Envisat scenes from two (2) adjacent descending satellite tracks (2005/6-2010/2011) acquired by European Space Agency (ESA), 23 ALOS-1 scenes from two (2) adjacent ascending tracks (2007-2011) acquired by Japan Aerospace Exploration Agency (JAXA), and 244 Sentinel-1A/B scenes from one (1) ascending track and one (1) descending track (2016-2020) acquired by European Space Agency (ESA). We also obtained 20 scenes of ascending ALOS-2 imagery (2014-2020) from three (3) neighboring tracks through our data proposal funded by JAXA, and 380 ascending Cosmo-SkyMed SAR scenes acquired during 2011-2015 through three (3) data proposals funded by Italian Space Agency (ASI). These Cosmo-SkyMed SAR data

are critical to bridge the data gap from 2011 to 2015. The radar satellite travels from approximately north to south and looks to the west during the descending track; and it travels from south to north and looks to the east during the ascending track. More detailed characteristics on SAR data used in this study and their spatial coverage can be found in Table 1 and Figure 1.

Table 1. SAR data characteristics in Greater Houston.

| Satellite | Band / Wavelength (cm) | Track No. | Heading (°) | Incidence angle (°) | Number of scenes | Date range (YYYYMMDD) |
|---|---|---|---|---|---|---|
| ERS | C / 5.6 | 212 | -166.8 | 23.1 | 18 | 19951121-20001219 |
| | C / 5.6 | 484 | -166.8 | 23.2 | 12 | 19930902-19971109 |
| Envisat ASAR | C / 5.6 | 212 | -165.6 | 23.2 | 27 | 20050129-20100925 |
| | C / 5.6 | 484 | -165.6 | 23.2 | 11 | 20060312-20080629 |
| ALOS-1 PALSAR | L / 23.6 | 175 | -10.3 | 38.7 | 12 | 20070926-20110104 |
| | L / 23.6 | 176 | -10.3 | 38.7 | 11 | 20070713-20110121 |
| COSMO-SkyMed | X / 3.1 | - | -11.3 | 23.9~26.6 | 380 | 20110613-20151225 |
| Sentinel-1 | C / 5.5 | 143 | 192.7 | 36.9 | 172 | 20160910-20200907 |
| | C / 5.5 | 34 | -10 | 39.3 | 72 | 20160927-20200602 |
| ALOS-2 PALSAR-2 | L / 23.6 | 53, 54,55 | -10.7~ -10.4 | 31.4~ 40.6 | 7/track | 20140918-20200122 |

## 2.3 InSAR Processing

We have processed each of the SAR datasets separately using MTI. To remove the topographic phase from the original interferograms, we have used Digital Elevation Model (DEM) from 1-arc-second (~30 m) Shuttle Radar Topography Mission (SRTM) data. We have utilized the Toolbox for Reducing Atmospheric InSAR Noise (TRAIN) package to produce coarse-resolution water-vapor measurements at times of SAR images and removed their effects in InSAR images (Bekaert et al., 2015). We have further suppressed the atmospheric artifact and baseline error by high-pass filtering of the unwrapped InSAR phase data in time, followed by low-pass filtering in space. The land surface deformation results are generated initially in radar coordinates, then orthorectified to the WGS84 universal traverse mercator (UTM) coordinate system and output as raster files. We have utilized ArcMap to manage and visualize all InSAR products.

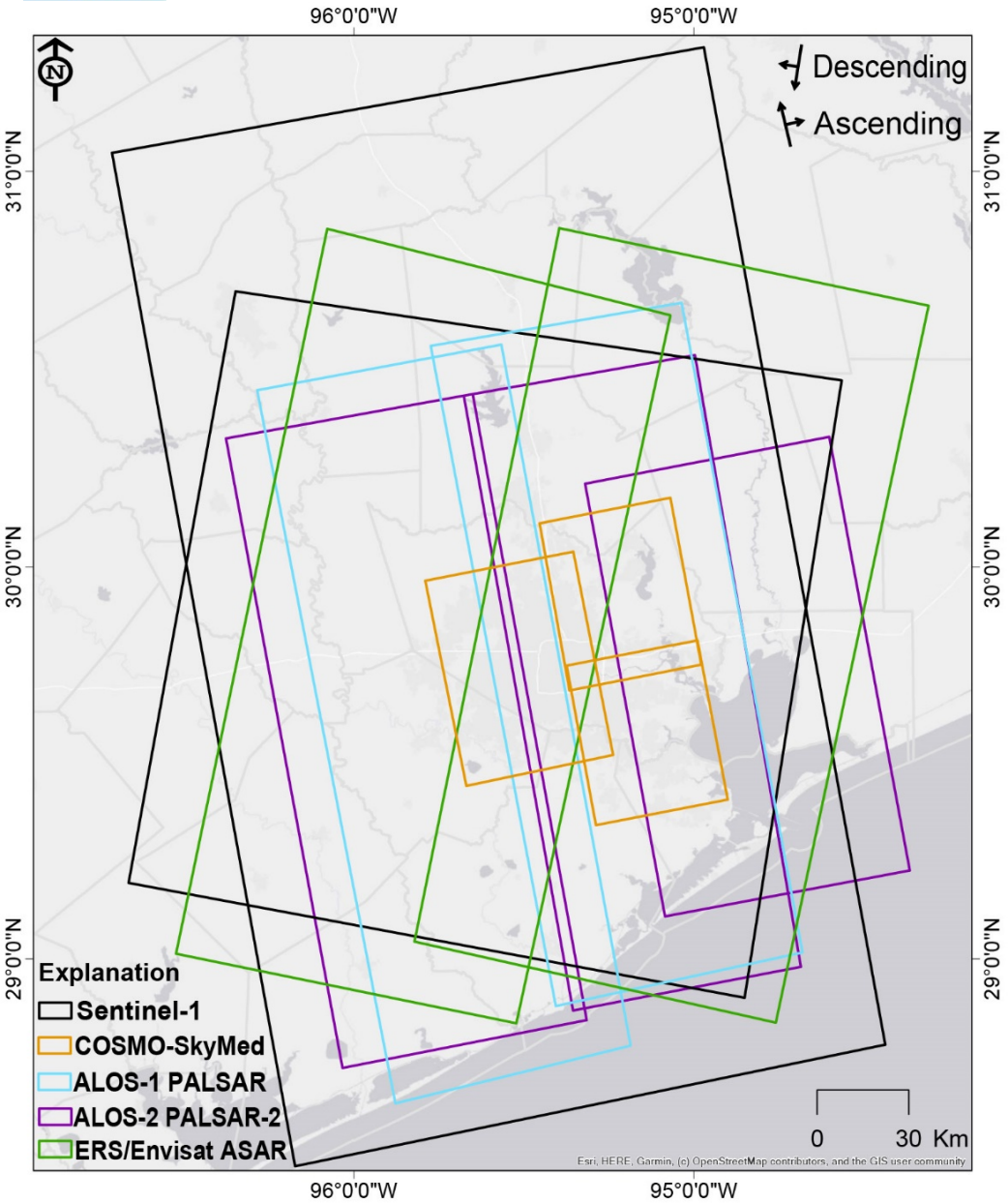


Figure 1. Spatial coverage of SAR data.

# 3.0 Project Results and Analyses

## 3.1 InSAR-derived Land Surface Deformation Maps

### 3.1.1 Average Line-Of-Sight land surface deformation maps

We have processed SAR images from five (5) different datasets (see Table 1) independently using the MTI processing and generated LOS land surface deformation rate maps over the GH region for the following observation periods: 2005-2010 (Envisat; Figure 3a), 2007-2011 (ALOS-1; Figure 3b), 2011-2015 (COSMO; Figure 4), 2016-2020 (Sentinel-1A/B; Figure 5), and 2014-2019 (ALOS-2; Figure 6). InSAR measurements from Envisat and two (2) neighboring ALOS-1 tracks show the overall distribution of deformation between 2005 and 2011 (Figure 3). The main broad-scale subsidence zone covers a northeastward elongated area of roughly 80 km by 30 km, which spans from Katy (western Harris County), across Jersey Village (northwestern Harris County), to The Woodlands (southern Montgomery County) and Spring (northern Harris County). This subsidence peaked at Spring and The Woodlands with a maximum subsidence rate of about 30 mm/yr (Figure 3) from 2005 through 2011. Compared with the measurement during the 1990s (Figure 2, Qu et al., 2015), the subsidence rate was reduced because of the reduction of groundwater withdrawal implemented in northern Harris County. Increased groundwater withdrawal has been transferred further north within the Jasper aquifer, and resulted in formation of new areas of water-level decline over Montgomery County. The second broad-scale area of subsidence is elongated northwestward, extending from Katy to Arcola (Fort Bend County). A relatively lower subsidence rate of about 15 mm/yr is observed over this feature from 2005 to 2011. The third large-scale subsidence feature is over Galveston County and the southern bound of Brazoria County with a relatively lower subsidence rate of ~10 mm/yr.

Subsidence rates vary both temporally and spatially during the following years. Figure 4 shows *preliminary* InSAR observation during 2011-2015 generated by five (5) frames of Cosmo-SkyMed (CSK) SAR data. The land surface deformation rate over Harris County during 2011-2015 decreased by about 10 mm/yr compared to the previous period from 2005 to 2011. But the results acquired by CSK might still contain artifacts for the following reasons, especially over northwestern Harris County. Limited by the large spatial baseline variations, the CSK datasets have to be processed separately by dividing them into several small stacks. The phase decorrelation induced by large spatial baselines rendered many CSK interferograms useless. A new proposal for additional data to densify the temporal coverage of Cosmo-SkyMed SAR images and enhance the reliability of CSK results is underway.

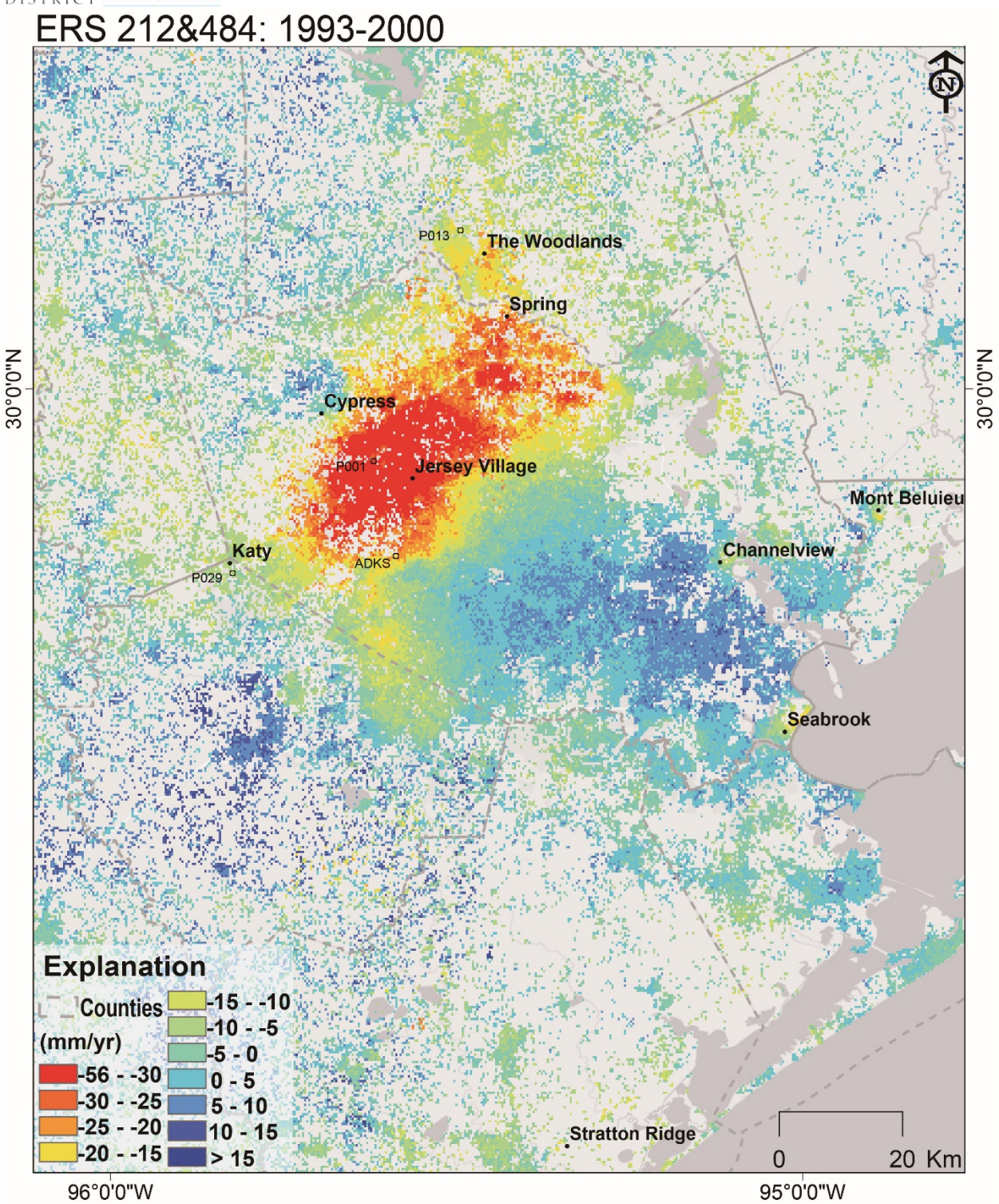


Figure 2. Average Line of Sight (LOS) land surface deformation map derived from ERS tracks 212 & 484.

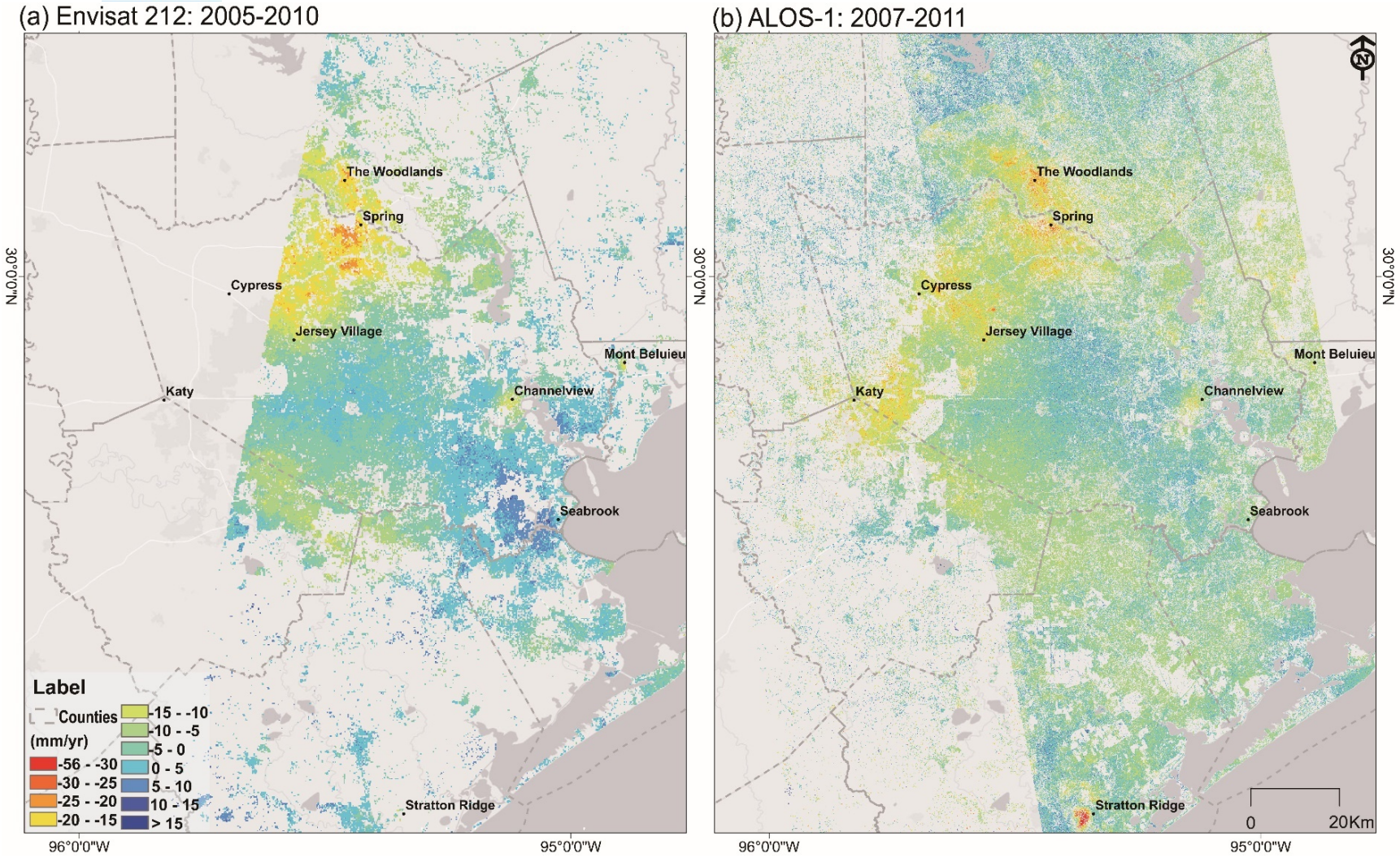


Figure 3. Average Line of Sight (LOS) land surface deformation maps derived from Envisat track 212 from 2005 through 2010 and ALOS-1 tracks 175 & 176 from 2007 through 2011.

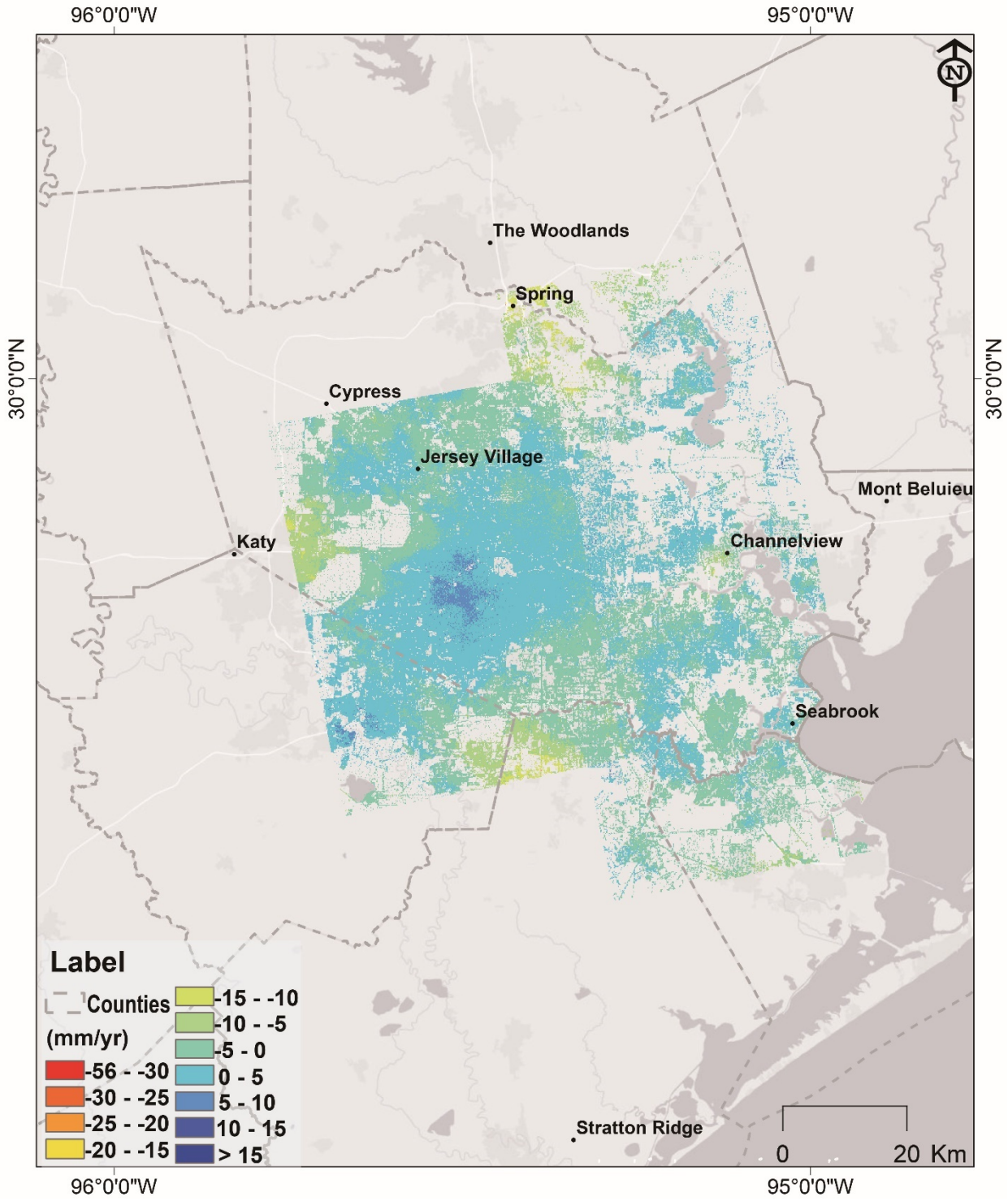


Figure 4. Preliminary average Line of Sight (LOS) deformation map derived from Cosmo-SkyMed (2011-2015).

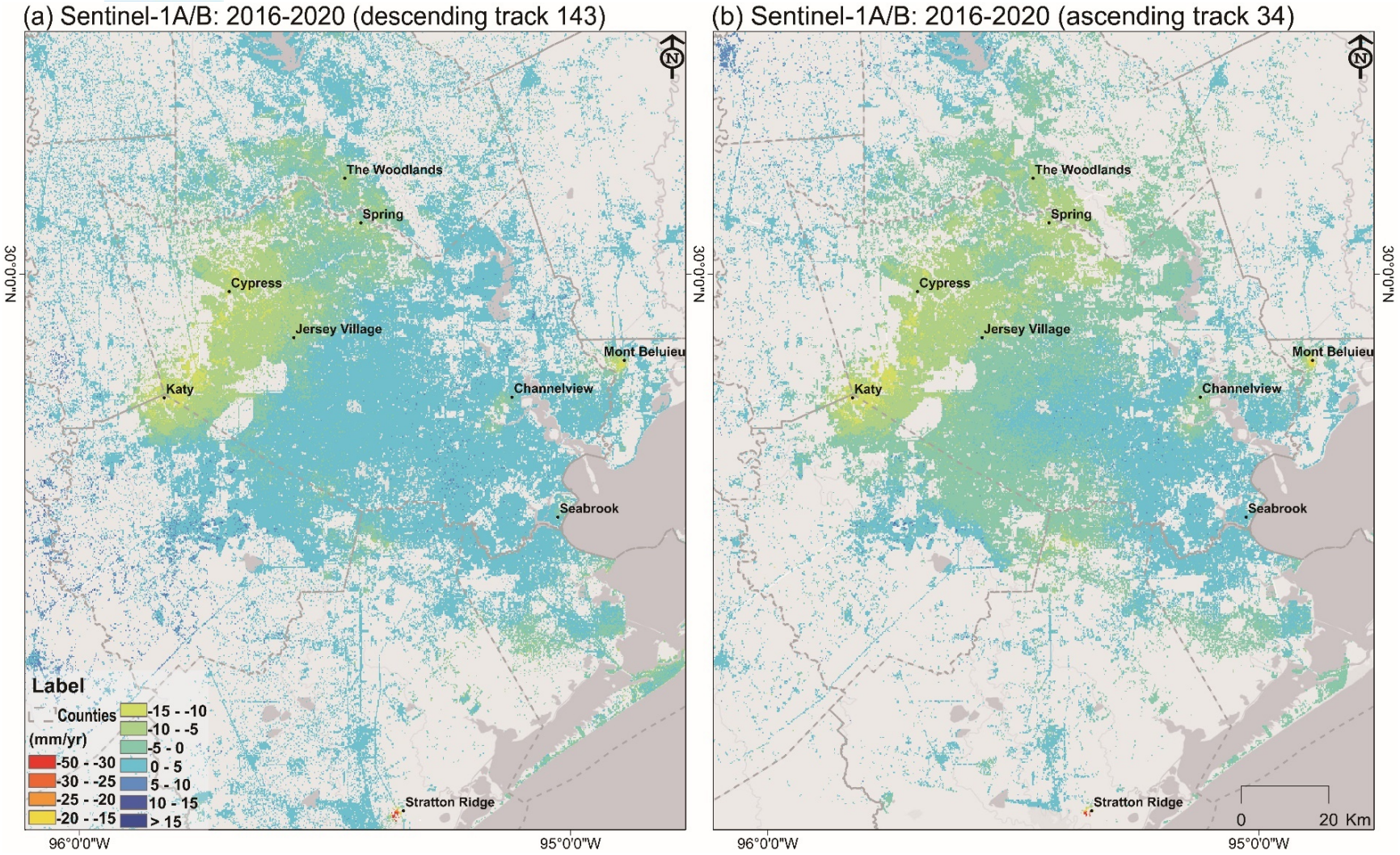


Figure 5. Average Line of Sight (LOS) deformation maps derived from Sentinel-1 A/B tracks (2016-2020).

From 2016 through 2020, the maximum rates of subsidence over Harris County appear to be 20 mm/yr, which was evidenced by both ascending and descending Sentinel-1A/B, as well as the ALOS-2 results (Figures 5-6). The maximum subsidence centers transferred from Spring in Harris County and The Woodlands in Montgomery County during 2005-2011 to Katy (Fort Bend County and northern areas in Harris County) no later than 2016 (Figure 5). The land surface deformation rate in The Woodlands decreased to 10 mm/yr during the Sentinel-1A/B period from 2016 to 2020. The land surface of the second broad-scale area of subsidence is still experiencing a relatively lower rate of 2-8 mm/yr from 2016 through 2020; however, localized subsidence with a rate of about 10 mm/yr was recognized at several communities in western Pearland. Both descending and ascending Sentinel-1 A/B datasets recognized both subsidence and uplift signals over Galveston County. Throughout the whole study period (i.e., 28 years), Channelview experienced subsidence with an average rate about 20 mm/yr.

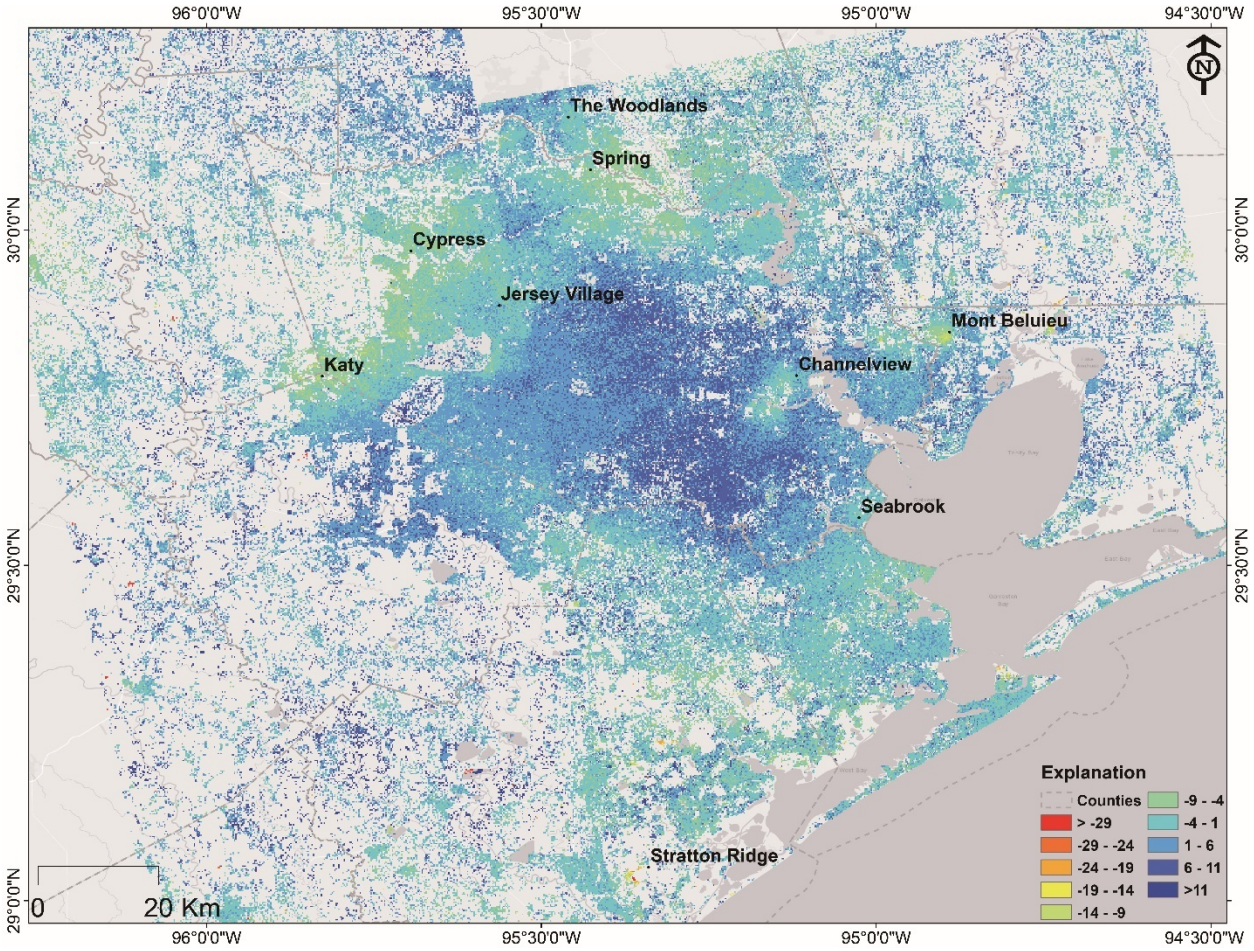


Figure 6. Average Line of Sight (LOS) deformation map derived from ALOS-2 tracks (2014-2019).

Although land surface deformation rates vary with locations, uplift is observed in the central and southeastern Harris County (up to 20 mm/yr) during the 1990s owing to effective groundwater regulation implementation. During more recent years, the pattern of uplift over Harris County is migrating from south to north and subsidence has migrated to the northern and western portions of Harris County. Much of the

land over central Harris County is experiencing very slight subsidence of 1-3 mm/yr, which agrees with natural rates of subsidence (Zhou et al. 2021).

### 3.1.2 Result validation between individual InSAR observations

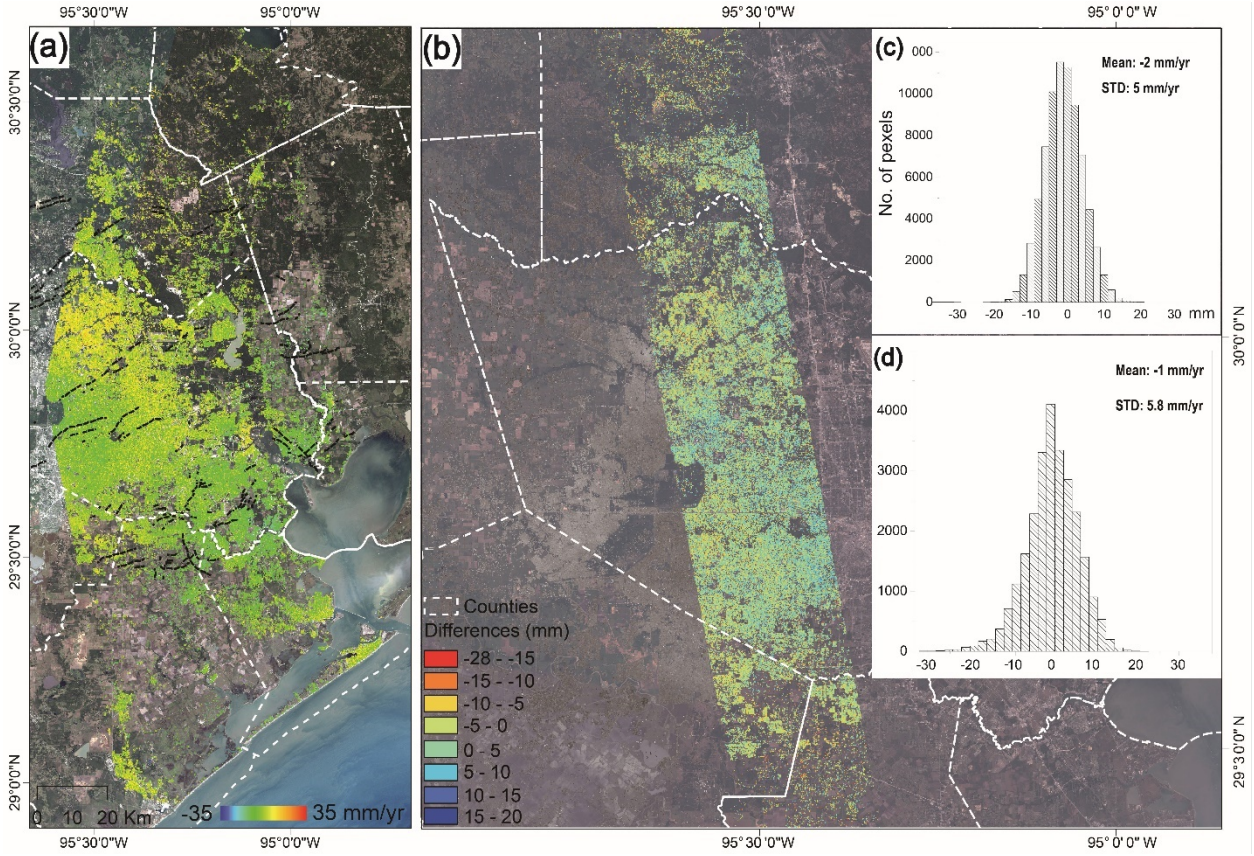


Figure 7. Differences in the vertical displacement derived from (a) ALOS-1 and Envisat, and (b) neighboring paths 175 and 176; (c) The corresponding histogram of (a); (d) The corresponding histogram of (b).

We have compared the InSAR-derived land surface deformation measurements using independent InSAR observations that cover the same area and span the same time interval. For the period of 2007 through 2010, we have independent InSAR measurements from Envisat and ALOS-1 (Figure 3). In addition, two (2) adjacent ALOS-1 tracks from 2007 to 2011 have an overlap (Figure 3b). We also have Sentinel-1A/B data from both ascending and descending tracks covering the GH region (Figure 5). In order to compare the vertical displacement rates from these datasets, we calculate two (2) new mean deformation rate maps spanning 2007 to 2010 from ALOS-1 and Envisat images. The InSAR derived deformation is measured along the SAR's LOS direction. The InSAR measurements from independence tracks are commonly transferred into the vertical direction according to the incidence angles to minimize the effects of imaging geometry when comparing two (2) InSAR measurements. As such, InSAR LOS measurements are projected into the vertical direction with respect to the corresponding incidence angles. Then, the overlapped parts of the displacement maps that span the same time interval are selected to compare the vertical deformation measurements between two (2) independent measurements. Figure 7a shows the

difference in the vertical displacement from the Envisat and ALOS-1 datasets (Figure 3). The standard deviation between these two (2) datasets is about 5 mm/yr (Figure 7c). Figure 7b shows the difference in vertical displacement from two (2) adjacent ALOS-1 tracks (track 175&176, Figure 3b). The standard deviation of the difference map is about 5.8 mm/yr (Figure 7d). Figure 8 shows the difference in vertical displacement between ascending and descending Sentinel-1A/B tracks (track 143&34, Figure 5). The standard deviation of the difference map is about 2.7 mm/yr (Figure 8b).

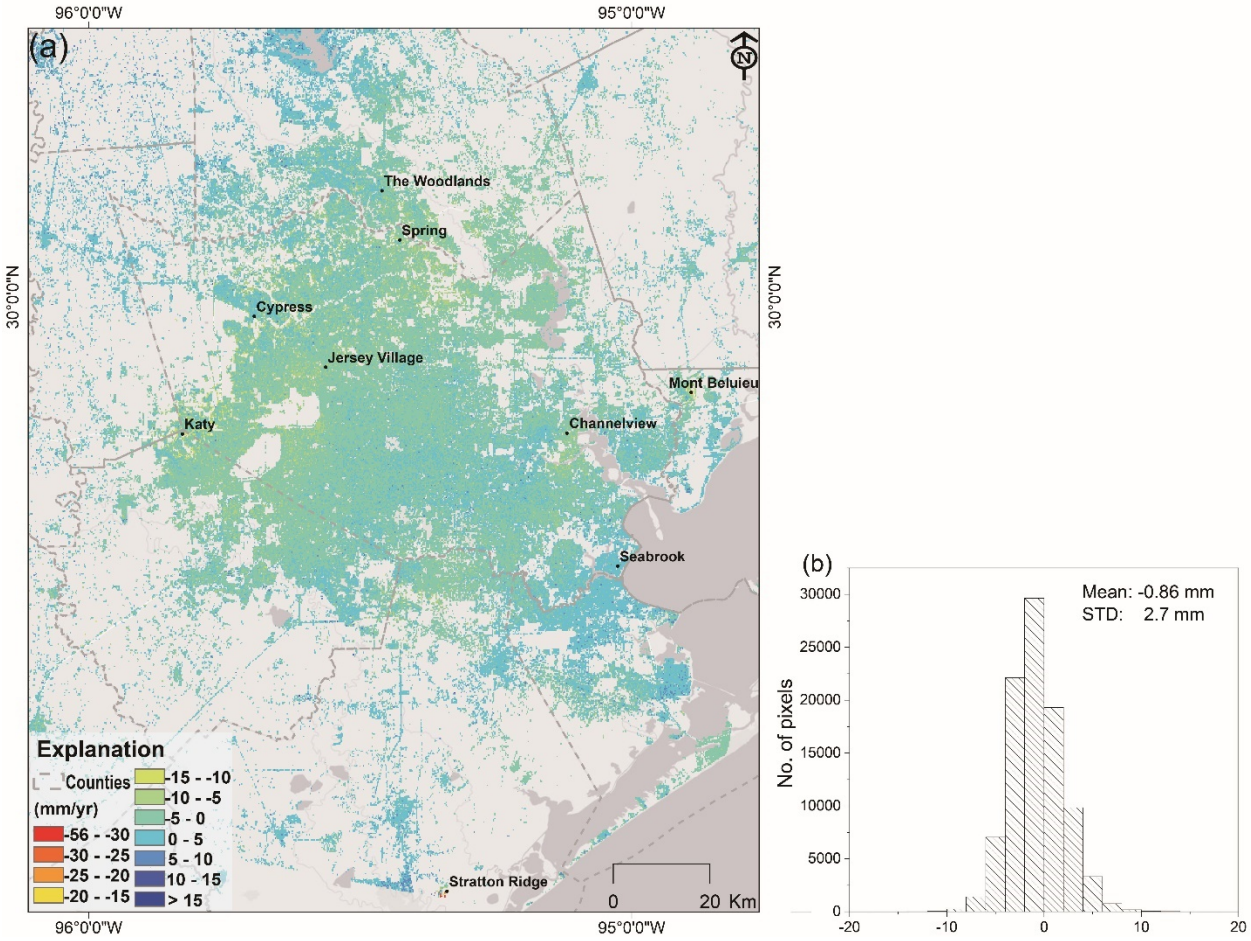


Figure 8. Differences in the vertical displacement between ascending and descending Sentinel-1A/B.

### 3.1.3 Result validation using GPS measurements

We next use measurements from PAM GPS stations to evaluate the results of the land surface deformation from MTI (Figure 9). We selected three (3) GPS stations located within the three (3) main subsidence areas: P001, P013 and P029. The 3-dimensional GPS measurements from stations P001, P013 and P029 are projected along the corresponding LOS directions according to the respective incidence angles. The average root means square error (RMSE) of the differences between InSAR and GPS measurements is about 10 mm, indicating a good agreement between InSAR-derived time series deformation measurements and daily/monthly GPS solutions. Time-series deformation from station P013, located in The Woodland area, shows a decreased rate of subsidence during the Sentinel-1A/B period,

while accelerated rate of subsidence was observed at stations P001 and P029 stations near Jersey Village and Katy, respectively.

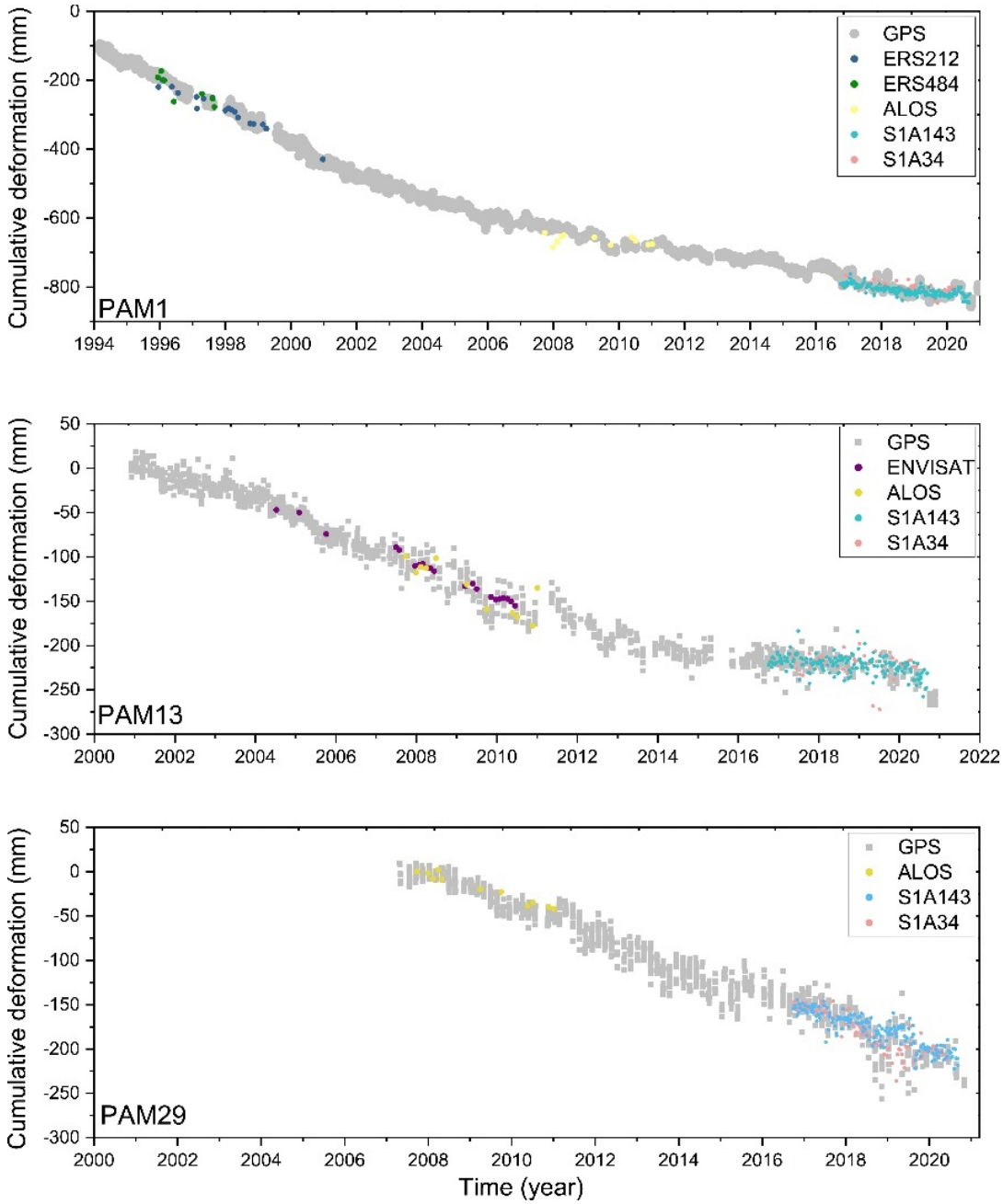


Figure 9. Comparison of InSAR-derived time-series deformation data with GPS station data.

## 3.2 Typical Subsidence Features

### 3.2.1 Local land subsidence caused by hydrocarbon exploration

Even though aquifer compaction due to groundwater extraction is the primary mechanism for regional subsidence over the GH area, oil and gas exploration and related production activities may also contribute to localized subsidence. Pressure relief in oil/gas production sites can lead to reservoir compaction and

ground surface subsidence above the reservoir. The first recognized ground deformation associated with fluid withdrawal was in the vicinity of the Goose Creek Oil Field (Pratt & Johnson, 1926), which remains subsiding for nearly a century to the present at a small rate (Qu et al., 2015). Barbers Hill is another prolonged active field where a large number of production wells are located. Our InSAR results from three (3) independent datasets (ERS, Envisat and Sentinel-1A/B) indicate continued subsidence of more than 20 mm/yr centered at the southeastern part of the oil field, where nearly eight hundred (800) active wells are distributed (Figure 10). This contrasts to the observed uplift over the oil field before 1970 (Holzer and Bluntzer, 1984). The subsidence center at Barbers Hill oil field nearly followed the distribution of working wells. Even though Holzer and Bluntzer (1984) attributed the relative uplift at Barbers Hill to salt dome activity, we can conclude that the present state of subsidence since 1992 was very likely caused by hydrocarbon exploration.

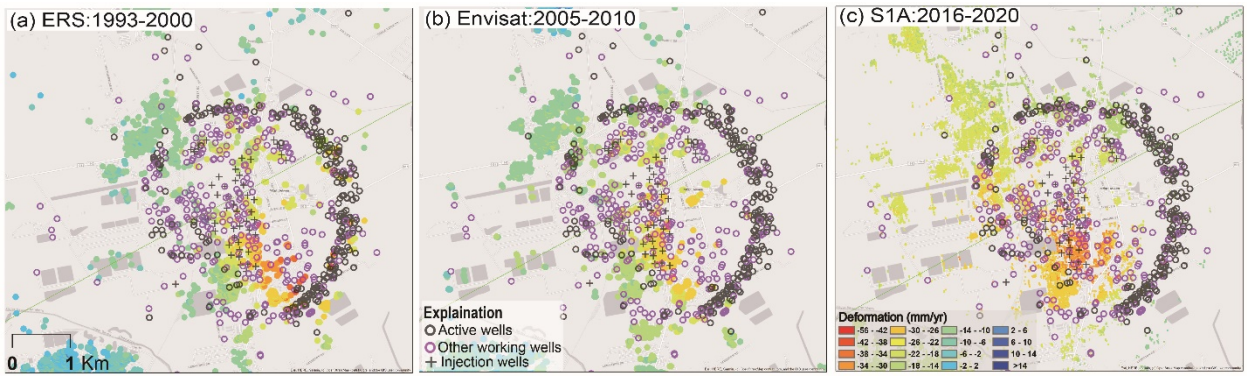


Figure 10. Time series evolution of the land surface elevation at Barbers Hill oil field, Mont Belvieu, from 1993 through 2020.

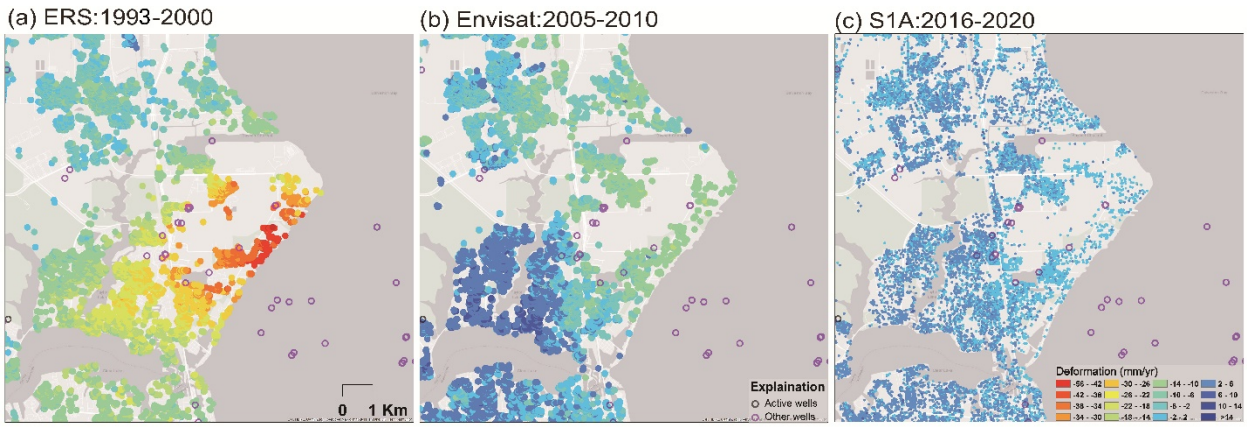


Figure 11. Time series evolution of the land surface elevation at Seabrook oil field using average Line of Sight (LOS) deformation maps from four independent datasets from 1993 through 2020.

Another example of land subsidence potentially related to hydrocarbon production is observed at the Seabrook oil field. An interesting result comes from the detected subsidence over the Seabrook oil field (Figure 11). A discrepancy in observed land surface deformation between InSAR and extensometer time series data during ERS period at the Seabrook extensometer site was observed by (Qu et al., 2015). The extensometer is located at the bottom of the Chicot Aquifer at a depth of 420.9 m (USGS, 2022). From

1990 through 2011, the compaction measurement at the Seabrook borehole extensometer essentially shows no deformation while InSAR measures subsidence at a rate ranging from 10 to 30 mm/yr. (Qu et al., 2015). The Chicot water-level altitude, on the contrary, exhibited a smooth increase during this period due to the groundwater regulation by HGSD since 1975 (Kasmarek et al., 2012; Yu et al., 2014). It should be noted that most of the groundwater wells in the GH area are drilled to depths ranging from 300 to 600 m and completed in the Chicot aquifer while the hydrocarbon wells are drilled to an average total depth deeper than 1300 m in the Houston area (Capital, 2017; Texas, 2022). In addition, the subsidence center at Seabrook nearly followed the distribution of hydrocarbon production wells from both land and sea (Figure 11). Therefore, the observed subsidence over the Seabrook oil field may be caused by hydrocarbon extraction. Furthermore, our InSAR measurements suggest a high subsidence rate of about 30 mm/yr in the 1990s (Figure 11a) and then a reduced subsidence rate of less than 10 mm/yr during 2005 through 2020 (Figure 11b). Our observations agree with the production activity of the wells at the Seabrook oil field over this period: most wells were drilled around 1985-1990, some wells stopped working around 2005-2010, and no active wells as of 2022 (Texas, 2022). Additional information on hydrocarbon production and wastewater injection volumes should be investigated to better understand the subsidence mechanism over the Seabrook oil field, though we interpret the main driver to be hydrocarbon extraction.

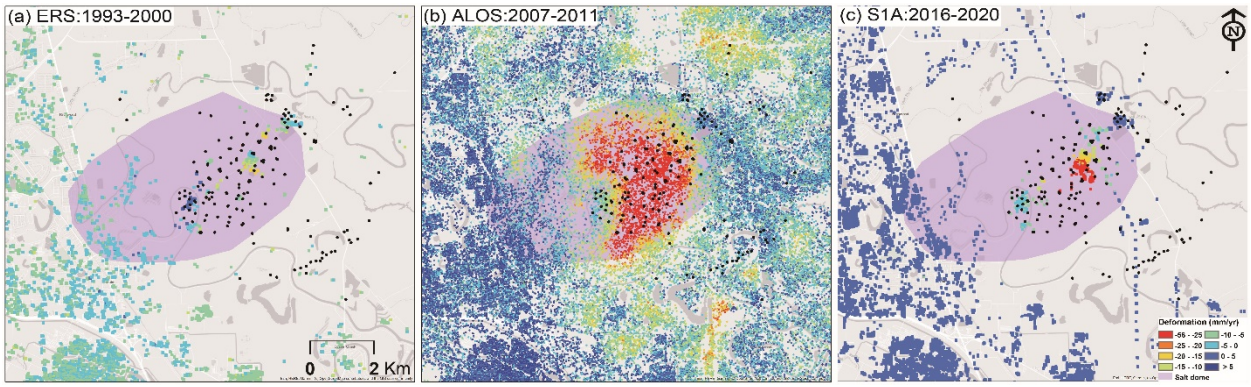


Figure 12. Average LOS deformation maps over Stratton Ridge oil field. (a) ERS; (b) ALOS-1; (c) Sentinel-1. Black dots represent hydrocarbon production wells (Texas, 2022). Light purple ellipsoids display the position of Stratton Ridge dome.

Our InSAR results indicate a localized area of subsidence with rates around 56 mm/yr over the Stratton Ridge oil field, located near Clute in Brazoria County, Texas (Figure 12b). The spatial extent of the subsidence cone matches the distribution of active wells located at the eastern part of Stratton Ridge oil field. The InSAR map from the ALOS dataset has much higher coherence than those from C-band ERS-1/2, Envisat and Sentinel-1A/B due to stronger penetration ability from L-band radar (Figure 12). Despite the low coherence of C-band data at a nonurban area, ERS and Sentinel-1A/B data still record similar results as that from ALOS. There is a high correlation between the spatial distribution of subsidence and hydrocarbon-related wells.

The Stratton Ridge salt dome is a large salt diapir located about 15 km from the currently active Strategic Petroleum Reserve Site at Bryan Mound, Texas (Rautman et al., 2006). It is roughly oval in outline, with its long axis oriented southwest to northeast (Figure 13) (Huffman Jr et al., 2004). Numerous shallow and cavern-related wells have been drilled on the flanks since about 1922 and produced between the 1950s and the 1970s. The caprock geometry of the Stratton Ridge salt dome is remarkable as the top of the eastern one-third of the Stratton Ridge dome is depressed at least 1,000 ft with respect to the western two-thirds (Figure 13b). Furthermore, within that structurally low eastern one-third area is a north-south elongated “basin” (Rautman et al., 2006). The subsidence cone at Stratton Ridge oil field, discovered by both ALOS and Sentinel-1A/B data, appears to present the same trend (i.e., down in the east and up in the west). This pattern of deformation agrees with the 3D model map of the Stratton Ridge salt dome that shows the geometry of the top of the caprock (Rautman et al., 2006). The vertical growth of the salt pillows creates pressure on the upward surface. Surface subsidence can thus occur above a shallow salt diapir due to the differential movement of the underlying salt. The subsidence cone here seems to be related to hydrocarbon/brine exploration or ongoing differential movement of individual salt spines.

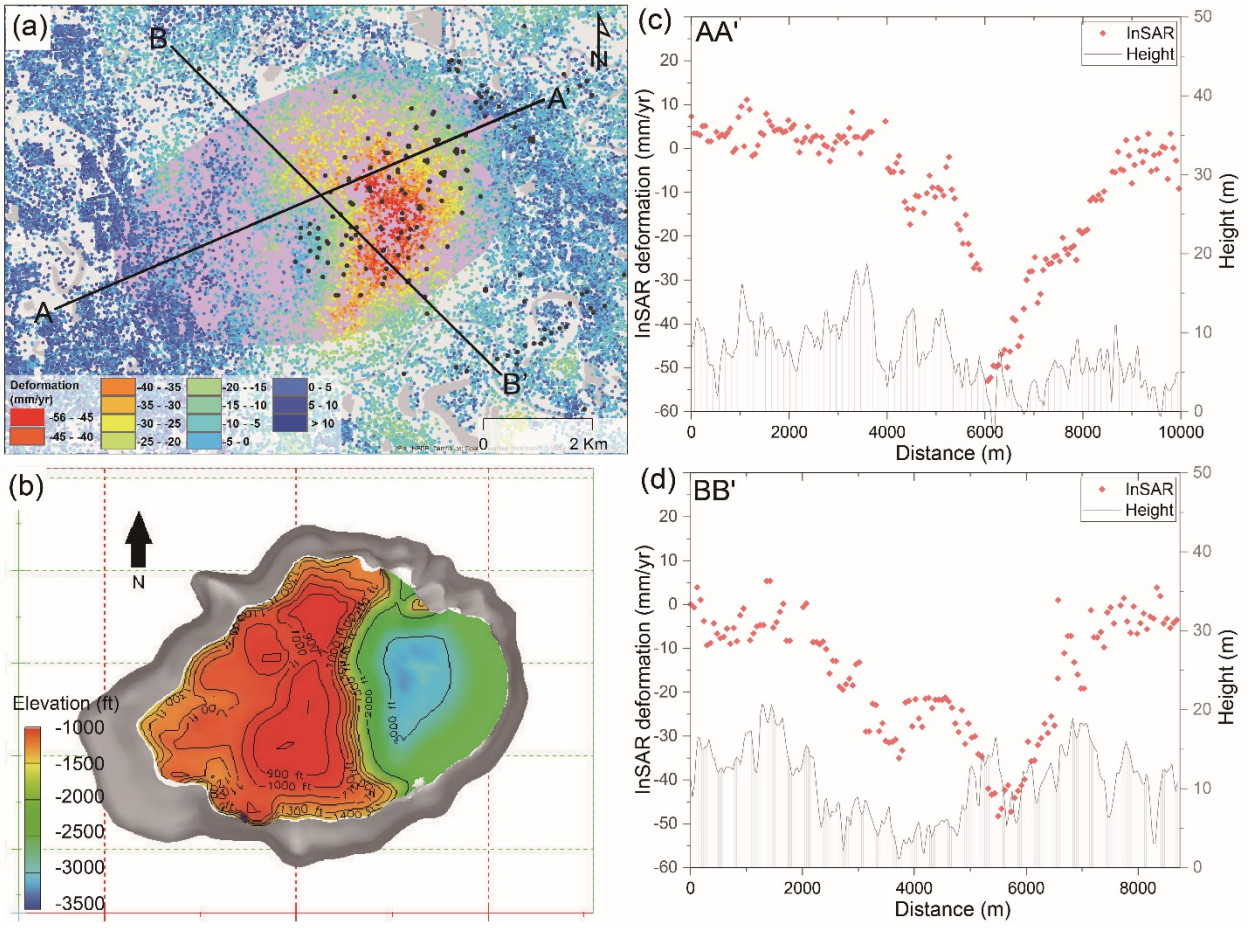


Figure 13. Average LOS deformation map and across-section profiles over Stratton Ridge oil field. (a) The subsidence map from MTI analysis of ALOS-1 data (2007-2011). The locations of wells over the salt dome are superimposed on the subsidence map; (b) 3D map of the Stratton Ridge salt dome, showing the geometry of the top of the caprock (Rautman et al., 2006); (a and d) Land deformation from ALOS-1 InSAR along the two (2) profiles whose positions are marked on (a). Gray lines indicate the surface elevation.

Underground storage facilities play a significant role in managing the delivery and supply chain of natural gas. Most underground gas storage facilities are located in depleted reservoirs in oil/gas fields, aquifers, and salt cavern deposits. Salt caverns that are leached or mined out of underground salt formations are perfect containers for underground gas storage because of their capabilities of high deliverability and quick replenishment, with 4% of the working gas capacity in the US in such facilities (Commission, 2004). Most salt cavern storage facilities have been developed in salt dome formations located along the Gulf Coast and the North Dayton salt dome gas storage facility in Liberty County, TX, which has been operating since 1986, is one of them (Texas, 2021).

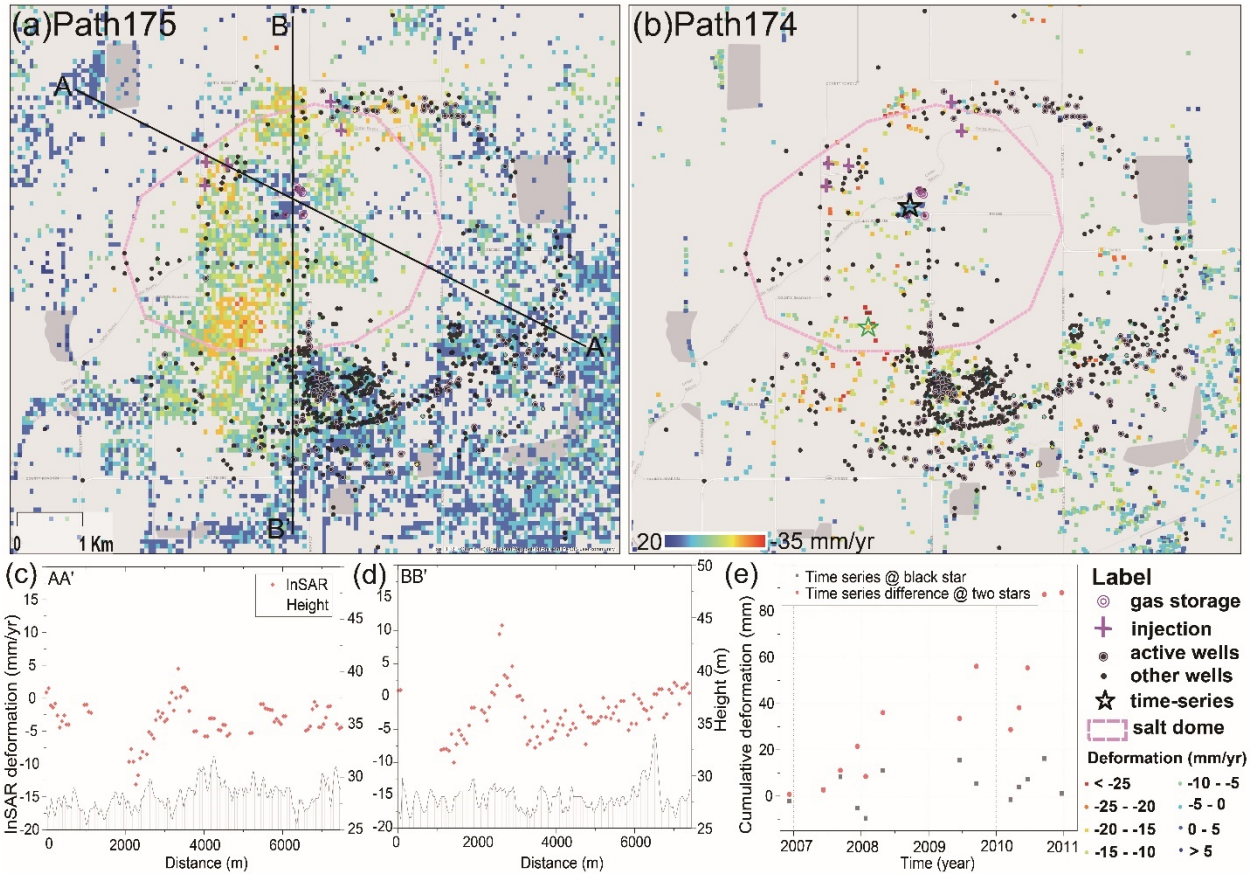


Figure 14. Average LOS deformation maps (2007-2011) over North Dayton gas field/salt dome. (a-b) enlarged average deformation maps (2007-2011) at the North Dayton salt dome from neighboring ALOS tracks 175 (a) and 174 (b). Light pink ellipsoids display the position of the salt dome. Purple circles represent storage wells, while the dense black dots show the distribution of hydrocarbon exploration wells. (c) and (d) show deformation and topographic height along profiles AA' and BB'. (e) time-series deformation (gray squares) at the position of the black star on (b), and time-series deformation difference (red dots) between the areas marked by black and green stars on (b).

During the circulated operations of injection/withdrawal into/from a salt cavern, the cavern's temperature change, coupled with the change in operating pressure, could change the effective stress on the cavern wall, leading to ground surface displacement (Figure 14). Our InSAR observations indicate the deformation over the North Dayton salt dome is complex. It includes a localized uplift feature occurs over the storage facilities and is surrounded by regional subsidence (Figure 14). Despite deformation of the cavern

fluctuations over time, time-series deformation at North Dayton gas field indicates a very slight uplift of about 20 mm from 2007 to 2011 (grey squares in Figure 14e). When analyzing the time-series deformation in the uplift area at the site of the wellbore (black star) in relation to the surrounding regional subsidence (green star), we discovered this feature had risen by approximately 90 mm during four years. The observed uplift fluctuates over time, responding to the seasonal nature of gas injection operations in summer (Figure 14e). We attribute the recognized localized uplift signal over the North Dayton salt dome gas storage facility to the circulated operations of injection/withdrawal into/from the salt cavern.

### 3.2.2 Transient & localized deformation features

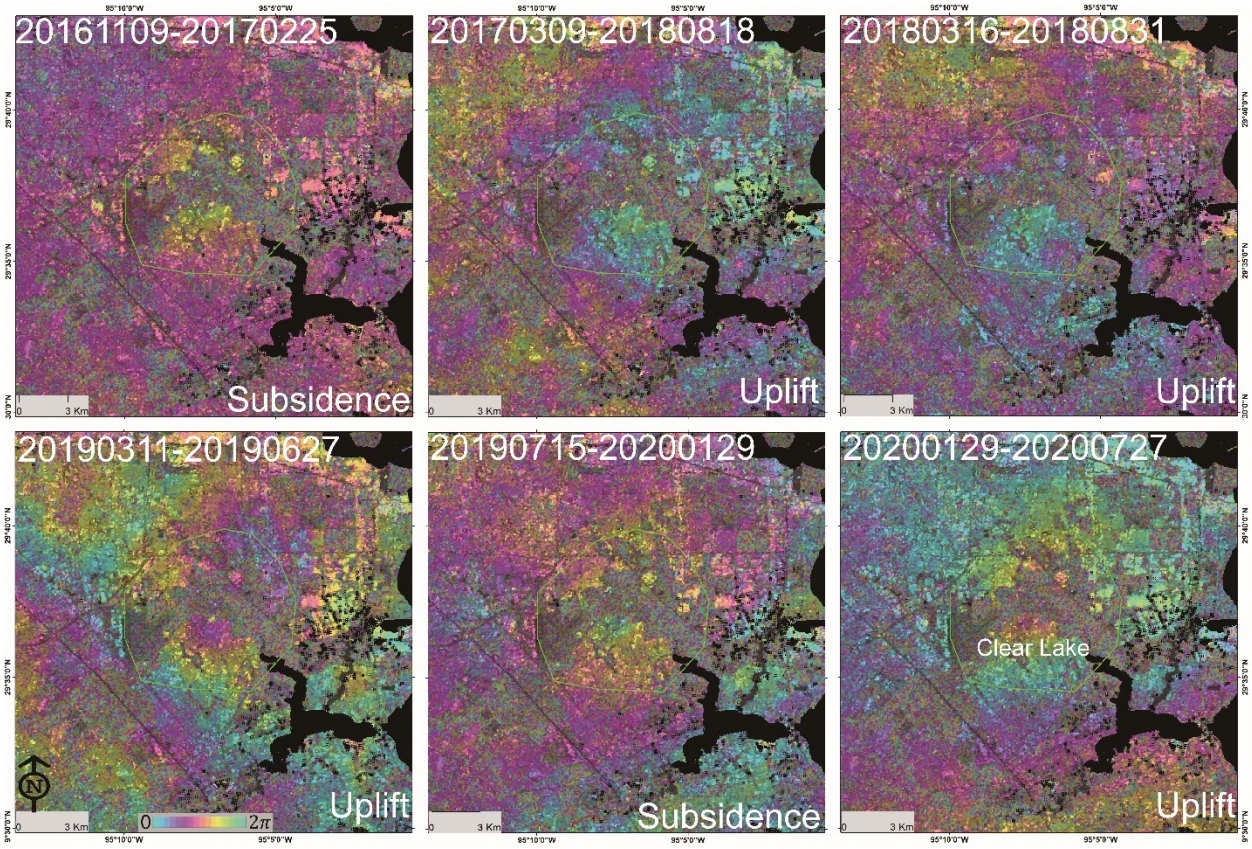


Figure 15. Interferograms over Clear Lake area from Sentinel-1 path 143. Each complete color cycle (i.e., blue, purple, red, orange, yellow, green, blue) represents a phase change of $2\pi$. Determine if the ground moved closer (uplift) or farther away (subsidence) from the satellite by matching how the colors change between the two points with the InSAR scale bar. If we take the boundary of the deformation feature, i.e., green polygon, as a reference, an increase in range (i.e., red, yellow, blue) signifies subsidence in the center of the green polygon, and a decrease in range (i.e., blue, yellow, red) indicates uplift.

We discovered (5) five transient deformation patterns through comprehensively analyzing interferograms from Sentinel-1A/B path 143, and the locations of the identified features are attached with this report. These transient displacements are localized and of short duration and therefore are rarely captured by MTI processing. Figure 15 presents an example of a transient deformation pattern showing selected interferograms with transient phase signals over the Clear Lake area. We should note that all listed interferograms have been verified by the contemporaneous interferograms. Surface subsidence of a few

millimeters occurred from 20161109 to 20170225, but switched to uplift during 20170309-20170818, 20180316-20180831, and 20190311-20190627. Subsidence resumed during 20190715-20200129, but uplift resumed during the period of 20200129-20200727 (Figure 15). The ground surface is considered silent during the rest of the periods, though we have not ruled out the possibility that deformation signals may have been masked by atmospheric artifacts. In order to understand the mechanism of these features, we explored the groundwater and hydrocarbon production activities over the Clear Lake area. An active oil/gas field, including many injections, storage and production wells, is located in the center of the observed deformation feature (Figure 16), suggesting a possible link to activities of hydrocarbon extraction or wastewater injection.

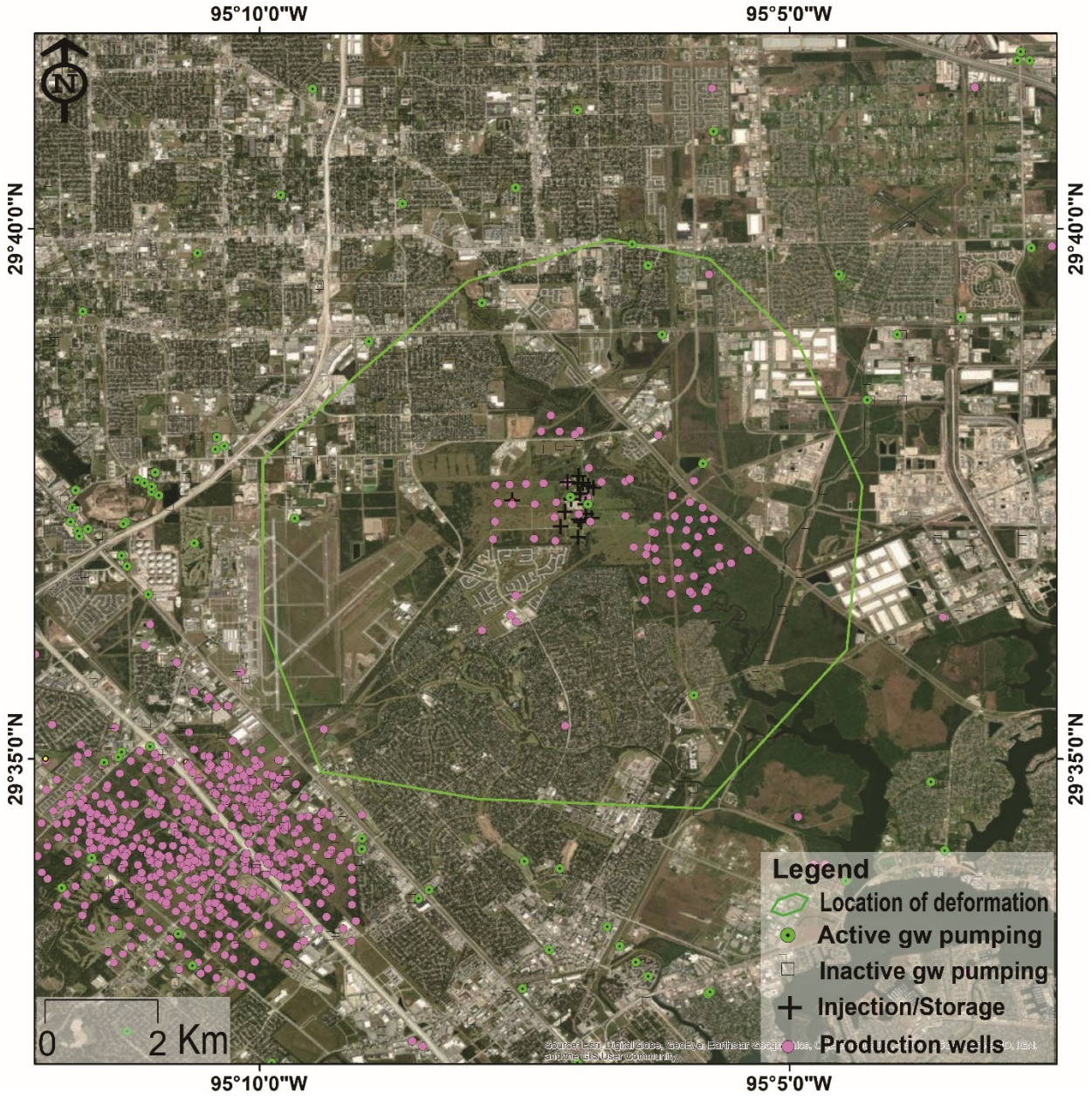

Figure 16. Distribution of groundwater and hydrocarbon production wells over the Clear Lake area.

## 3.3 Faulting activity mapped by ALOS & Sentinel-1A/B

Figure 17 shows enlarged deformation maps over northwestern Houston from ascending and descending Sentinel-1A/B tracks as well as two (2) adjacent ALOS-1 paths. From the long-term velocity maps, we can see numerous sharp phase discontinuities along fault traces over the GH region, especially in the northern areas (i.e., north Harris County and south Montgomery County), seen as sharp color contrasts (noted by the pink arrows in Figure 17a-b). These areas are covered by both ascending and descending Sentinel-1A/B tracks, and both independent tracks show remarkably consistent velocity steps and gradients (Figure 17a-b). Based on the inference that steep phase discontinuities should be caused by the ongoing differential movement of two (2) sides of faults, fault traces can be depicted along the steep phase discontinuities (Figure 17c-d). At least three (3) broad-scale active faulting zones can be imaged over the northern GH region: the Hockley fault System, the Big Barn fault System and the Conroe Fault System, all within the larger Hockley-Conroe Fault System that runs northeast from the town of Hockley to the city of Conroe. Our InSAR-mapped discontinuity lines (2007-2011, 2016-2020) match the light detection and ranging (LiDAR)-mapped fault traces (2001-2008) at some points, indicating our results are consistent with the faults mapped by LiDAR (purple lines in Figure 17). We should note that InSAR-mapped fault traces indicate the faults were active during that observed period, i.e., the ALOS-mapped faults illustrate these fault segments were active during 2007 and 2011, while the Sentinel-1 faults represent faults that were active during 2016 and 2020.

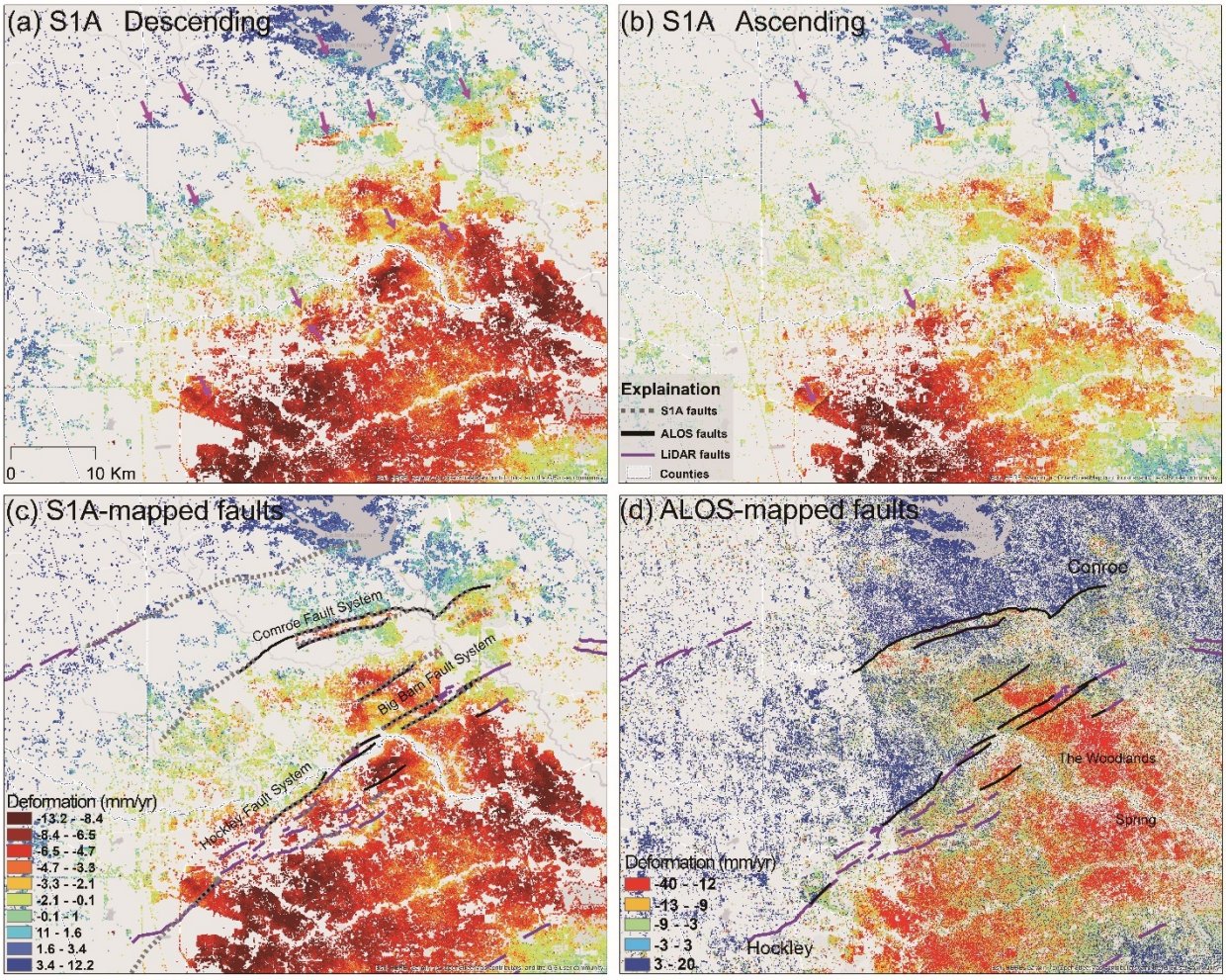


Figure 17. Faulting activity mapped by ALOS & Sentinel-1A/B in northwestern Harris County and southern Montgomery County. (a) Enlarged deformation maps from two Sentinel-1 paths: (a) Descending path; (b) Ascending path. The pink arrows in (a) and (b) represent zones of high deformation velocity gradient (differential movement); (c) Descending Sentinel-1 path. The purple lines represent the faults mapped by LiDAR, while newly revealed fractures by our Multi-temporal InSAR (MTI) processing are in black dashed lines (Sentinel-1) and gray lines (ALOS-1); (d) Enlarged deformation map from ALOS-1 (2007-2011).

The Hockley Fault and Big Barn fault were extensively investigated with a variety of geophysical methods to delineate the fault and define the geology of the upper rock units (Han, 2013; Khan et al., 2013; Minteer, 2018; Saribudak, 2010, 2012; Saribudak et al., 2018). Sharp contrasts in InSAR deformation map from the upthrown side (smaller deformation) of the fault to the downthrown side (larger deformation) are evident at all their field sites. Thus, we confirm that the discontinuities in the MTI-derived images correspond nicely to the surface ruptures. Fugro Consultants, Inc. and Tolunay-Wong Engineers, Inc acknowledged the presence of faulting and mapped where the faulting occurred through their field investigations over the Big Barn Fault System (Fugro Consultants, 2012; Tolunay-Wong Engineers, 2014). The surface scarps published by these two (2) companies based on their geological survey for the purpose of designing a network of water pipelines are consistent with the InSAR-mapped fault traces at the Big Barn fault. The Conroe Fault was mentioned in a field trip guide book published by the Houston Geological Society that

indicated that there was no movement of the Conroe Fault between 1985 and 1987, while the rate of movement was 18 mm/yr in 1987 (Campbell, 2018). Damage to a swimming pool at the Conroe Aquatics Center, which is located on the InSAR-mapped fault line, was reported early in 2018, indicating the reactivation of the Conroe Fault (Dominguez, 2018).

## 3.4 Other Findings

Integrating InSAR, GPS, and extensometer measurements provide further insights into the source of the observed subsidence. We find the existence of a large disagreement between the GPS observations and the measurements from extensometer and InSAR time-series at ADKS-CORS, located in western Houston at the southeastern side of the Addicks Reservoir (Figure 18). The extensometer measures aquifer compaction between 6 m below the land surface and the concrete plug at the bottom of the borehole, which is the top of the Burkeville confining layer (549 m deep) at ADKS-CORS (Figure 19), while the GPS measures the displacement of the concrete plug. Our InSAR time-series deformation measurements indicate about 40 cm total subsidence at the ADKS-CORS site (Figure 18) from 1993-2020. That amount is consistent with extensometer compaction measurements. However, the GPS vertical time-series data at this site had little to no vertical motion before 2013 (Figure 18). Based on the combined InSAR, GPS, and extensometer measurements, we attribute the deformation at ADKS-CORS to the compaction of developed shallow aquifers (i.e., Chicot and Evangeline). However, slight subsidence has occurred at ADKS-CORS since 2013, and the subsidence rate appeared to be accelerating in 2020.

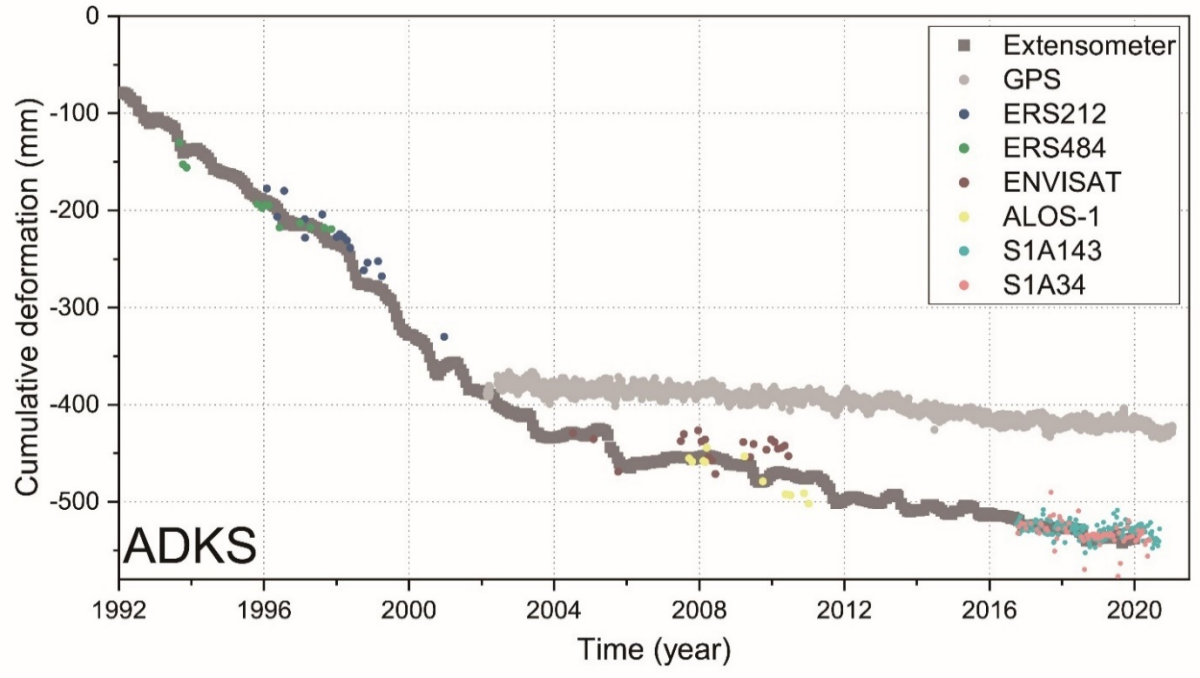


Figure 18. Time-series deformation of ADKS-CORS using data from InSAR, extensometer, and GPS station.

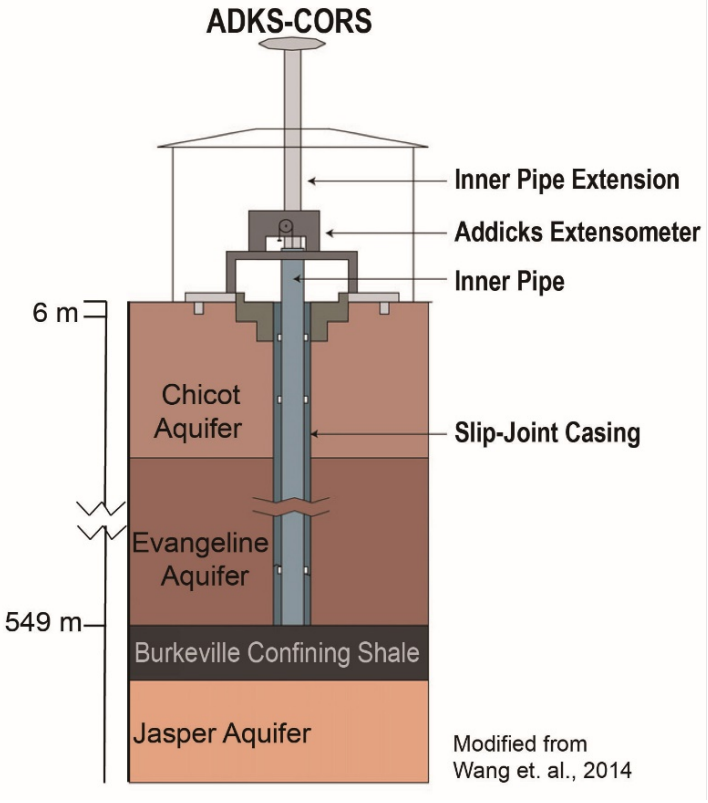


Figure 19. Diagrammatic sketch of the Addicks extensometer and co-located GPS station in Houston, Texas.

# 4.0 Project Conclusions

This project provides a comprehensive analysis about temporal and spatial land deformation over GH using the MTI technique. Through combining both PSInSAR and SBAS approaches, MTI can increase the spatial density of usable signal, allowing the identification of persistent scatterers (PSs) that dominate the scattering from the resolution element and slowly-varying filtered phase (SFP) pixels whose phases, when filtered, decorrelate little over short time intervals. All of the available SAR images, including Envisat (2005-2010), Sentinel-1 (2016-2020), ALOS-1 (2007-2011), ALOS-2 (2014-2019), and Cosmo-SkyMed (2011-2015) datasets have been used to unravel the characteristics of ground deformation of the GH from 2005 to 2020. Using GPS and extensometer observations, we report that the accuracy of our InSAR measurements of long-term subsidence can reach 2-11 mm/yr.

Deformation of the Houston area can generally be characterized as subsidence in the northwest and uplift in the southeast. Subsidence rates in the northwest decreased from about 53 mm/yr during the 1990s to around 30 mm/yr during 2005-2011. The maximum subsidence rates of about 20 mm/yr were in the western Houston region during later periods. The maximum subsidence centers transferred from Spring in Harris County and The Woodlands in Montgomery County during 2005-2011 to Katy, located in Fort Bend and Harris counties sometime between January 2011 and September 2016.

Land subsidence over the GH is not solely attributed to a single component, and the mechanisms are complicated, including the combined effects of groundwater and hydrocarbon extraction, tectonic process, and others. Besides the regional deformation patterns, localized subsidence from 1993 through 2020 can be spotted at many locations, including four (4) significant features with an average subsidence rate near or greater than 20 mm/yr: Stratton Ridge oil field, Mont Belvieu, Seabrook, and Channelview. Aquifer compaction due to groundwater withdrawal is still considered to be the primary driver of subsidence and hydrocarbon withdrawal in localized areas may be another driver of the observed surface deformation in the GH area. In addition, InSAR results have enabled us to identify and map fault fractures according to the steep phase discontinuities caused by the differential movement of two blocks of faults from InSAR velocity maps. Finally, based on the combined InSAR, GPS, and extensometer measurements, we conclude that the subsidence at ADKS has been attributed to the compaction of shallow aquifers.

# 5.0 Acknowledgements

This work was supported by the Harris-Galveston Subsidence District (HGSD) Fort Bend Subsidence District (FBSD), NASA NISAR Science Team [80NSSC19K1491], and the Shuler-Foscue Endowment at Southern Methodist University. We thank Ashley Greuter and Michael Turco of HGSD for the outstanding programmatic guidance throughout the investigation, and their constructive comments that improved the quality of this report.

# 6.0 References

Amelung, F., Galloway, D.L., Bell, J.W., Zebker, H.A., Laczniak, R.J., 1999. Sensing the ups and downs of Las Vegas: InSAR reveals structural control of land subsidence and aquifer-system deformation. Geology 27, 483-486.

Ashworth, J.B., 1995. Aquifers of Texas. Texas Water Development Board, Austin, Texas.

Baker Jr, E., 1979. Stratigraphic and hydrogeologic framework of part of the coastal plain of Texas. Texas Department of Water Resources, Austin, Texas.

Baker Jr, E., 1986. Hydrology of the Jasper aquifer in the southeast Texas Coastal Plain. Texas Department of Water Resources Austin, Texas.

Bawden, G.W., Johnson, M.R., Kasmarek, M.C., Brandt, J., Middleton, C.S., 2012. Investigation of land subsidence in the Houston-Galveston region of Texas by using the global positioning system and interferometric synthetic aperture radar, 1993-2000. US Geological Survey Scientific Investigations Report 2012-5211, p. 88.

Bawden, G.W., Thatcher, W., Stein, R.S., Hudnut, K.W., Peltzer, G., 2001. Tectonic contraction across Los Angeles after removal of groundwater pumping effects. Nature 412, 812.

Bekaert, D., Hooper, A., Wright, T., 2015. A spatially variable power law tropospheric correction technique for InSAR data. Journal of Geophysical Research: Solid Earth 120, 1345-1356.

Berardino, P., Fornaro, G., Lanari, R., Sansosti, E., 2002. A new algorithm for surface deformation monitoring based on small baseline differential SAR interferograms. IEEE transactions on geoscience and remote sensing 40, 2375-2383.

Buckley, S.M., Rosen, P.A., Hensley, S., Tapley, B.D., 2003. Land subsidence in Houston, Texas, measured by radar interferometry and constrained by extensometers. Journal of geophysical research: solid earth 108.

Campbell, M.D.C., M. David, Wise, Henry M., 2018. Growth Faulting and Subsidence in the Houston, Texas Area: Guide to the Origins, Relationships, Hazards, Potential Impacts and Methods of Investigation: An Update. Journal of Geology and Geoscience 2, 1-53.

Capital, E.a., 2017. The Depth of Oil Wells.

Chaussard, E., Bürgmann, R., Shirzaei, M., Fielding, E.J., Baker, B., 2014. Predictability of hydraulic head changes and characterization of aquifer-system and fault properties from InSAR-derived ground deformation. Journal of Geophysical Research: Solid Earth 119, 6572-6590.

Cigna, F., Osmanoğlu, B., Cabral-Cano, E., Dixon, T.H., Ávila-Olivera, J.A., Garduño-Monroy, V.H., DeMets, C., Wdowinski, S., 2012. Monitoring land subsidence and its induced geological hazard with Synthetic Aperture Radar Interferometry: A case study in Morelia, Mexico. Remote Sensing of Environment 117, 146-161.

Commission, F.E.R., 2004. Underground Natural Gas Storage, Current state of and issues concerning. Federal Energy Regulatory Commission.

Coplin, L.S., Galloway, D., 1999. Houston-Galveston, Texas-Managing coastal subsidence. Land subsidence in the United States: US Geological Survey Circular 1182, 35-48.

Dominguez, C., 2018. Fault line-damaged Conroe water park to open for one last summer. The Courier of Montgomery County.

Fattahi, H., Amelung, F., 2016. InSAR observations of strain accumulation and fault creep along the Chaman Fault system, Pakistan and Afghanistan. Geophysical Research Letters 43, 8399-8406.

Fattahi, H., Simons, M., and Agram, P., 2017. InSAR time-series estimation of the ionospheric phase delay: and extension of the split range-spectrum technique. IEEE Trans. Geosci. Remote Sensing 55.

Ferretti, A., Fumagalli, A., Novali, F., Prati, C., Rocca, F., Rucci, A., 2011. A new algorithm for processing interferometric data-stacks: SqueeSAR. IEEE transactions on geoscience and remote sensing 49, 3460-3470.

Ferretti, A., Prati, C., Rocca, F., 2001. Permanent scatterers in SAR interferometry. IEEE Transactions on geoscience and remote sensing 39, 8-20.

Fruneau, B., Sarti, F., 2000. Detection of ground subsidence in the city of Paris using radar interferometry: isolation of deformation from atmospheric artifacts using correlation. Geophysical Research Letters 27, 3981-3984.

Fugro Consultants, I., 2012. Geologic fault delineation study SJRA Distribution Lines-Route W1 San Jacinto River Authority Montgomery County, TX. Fugro Consultants, Inc. Report No. 04.12110014-9.

Galloway, D.L., Bawden, G.W., Leake, S.A., Honegger, D.G., 2008. Land Subsidence Hazards, in: Baum, R.L., Galloway, Devin L, Harp, Edwin L (Ed.), Landslide and land subsidence hazards to pipelines. Geological Survey (US).

Han, X., 2013. Integrated remote sensing and geophysical study of the Hockley fault in Harris and Montgomery Counties, Texas. University of Houston.

Holzer, T.L., Bluntzer, R.L., 1984. Land Subsidence Near Oil and Gas Fields, Houston, Texas a. Groundwater 22, 450-459.

Holzer, T.L., Galloway, D.L., 2005. Impacts of land subsidence caused by withdrawal of underground fluids in the United States. Humans as geologic agents 16, 87-99.

Hooper, A., 2008. A multi-temporal InSAR method incorporating both persistent scatterer and small baseline approaches. Geophysical Research Letters 35, L16302.

Hooper, A., Zebker, H., Segall, P., Kampes, B., 2004. A new method for measuring deformation on volcanoes and other natural terrains using InSAR persistent scatterers. Geophysical research letters 31, L23611.

Huffman Jr, A.C., Kinney, S.A., Biewick, L., Mitchell, H.R., Gunther, G.L., 2004. Gulf coast geology (GCG) online--miocene of southern Louisiana.

Kasmarek, M.C., Johnson, M.R., Ramage, J.K., 2010. Water-level altitudes 2010 and water-level changes in the Chicot, Evangeline, and Jasper aquifers and compaction 1973–2009 in the Chicot and Evangeline

aquifers, Houston-Galveston region, Texas. U.S. Geological Survey Scientific Investigations Map 3138, p. 17.

Kasmarek, M.C., Johnson, M.R., Ramage, J.K., 2012. Water-level Altitudes 2012, and Water-level Changes in the Chicot, Evangeline, and Jasper Aquifers and Compaction 1973-2011 in the Chicot and Evangeline Aquifers, Houston-Galveston Region, Texas. US Department of the Interior, US Geological Survey Scientific Investigations Map 3230, pp. 17 p., 16 sheets.

Kearns, T.J., Wang, G., Turco, M., Welch, J., Tsibanos, V., Liu, H., 2018. Houston16: A stable geodetic reference frame for subsidence and faulting study in the Houston metropolitan area, Texas, US. Geodesy and Geodynamics.

Khan, S.D., Stewart, R.R., Otoum, M., Chang, L., 2013. A geophysical investigation of the active Hockley Fault System near Houston, Texas. Geophysics 78, B177-B185.

Kim, J.-W., Lu, Z., Jia, Y., Shum, C., 2015. Ground subsidence in Tucson, Arizona, monitored by time-series analysis using multi-sensor InSAR datasets from 1993 to 2011. ISPRS Journal of Photogrammetry and Remote Sensing 107, 126-141.

Kim, S.W., Lee, C.W., Song, K.Y., Min, K., Won, J.S., 2005. Application of L-band differential SAR interferometry to subsidence rate estimation in reclaimed coastal land. International journal of remote sensing 26, 1363-1381.

Lu, Z., Danskin, W.R., 2001. InSAR analysis of natural recharge to define structure of a groundwater basin, San Bernardino, California. Geophysical Research Letters 28, 2661-2664.

Lu, Z., Dzurisin, D., 2014. InSAR imaging of Aleutian volcanoes, InSAR Imaging of Aleutian Volcanoes. Springer, pp. 87-345.

Martin, A., Whiteman, C.D., 1999. Hydrology of the coastal lowlands aquifer system in parts of Alabama, Florida, Louisiana, and Mississippi. US Department of the Interior, US Geological Survey.

Massonnet, D., Rossi, M., Carmona, C., Adragna, F., Peltzer, G., Feigl, K., Rabaute, T., 1993. The displacement field of the Landers earthquake mapped by radar interferometry. Nature 364, 138.

Minteer, D., 2018. A Geophysical Delineation of A Normal Fault Within the Gulf Coastal Plain, Montgomery County, Texas, Geology. Stephen F. Austin State University.

Mora, O., Mallorqui, J.J., Broquetas, A., 2003. Linear and nonlinear terrain deformation maps from a reduced set of interferometric SAR images. IEEE Transactions on Geoscience and Remote Sensing 41, 2243-2253.

Morton, R.A., 2003. An overview of coastal land loss: with emphasis on the Southeastern United States. U.S. Geological Survey Open File Report 03-337, p. 24.

Pratt, W.E., Johnson, D.W., 1926. Local subsidence of the Goose Creek oil field. The Journal of Geology 34, 577-590.

Qu, F., Lu, Z., Kim, J.-W., Zheng, W., 2019. Identify and Monitor Growth Faulting Using InSAR over Northern Greater Houston, Texas, USA. Remote Sensing 11, 1498.

Qu, F., Lu, Z., Zhang, Q., Bawden, G.W., Kim, J.-W., Zhao, C., Qu, W., 2015. Mapping ground deformation over Houston–Galveston, Texas using multi-temporal InSAR. Remote Sensing of Environment 169, 290-306.

Qu, F., Zhang, Q., Lu, Z., Zhao, C., Yang, C., Zhang, J., 2014. Land subsidence and ground fissures in Xi'an, China 2005–2012 revealed by multi-band InSAR time-series analysis. Remote sensing of environment 155, 366-376.

Rautman, C.A., Snider, A.C., Looff, K.M., 2006. Geologic technical assessment of the Stratton Ridge salt dome, Texas, for potential expansion of the US strategic petroleum reserve. Sandia National Laboratories (SNL), Albuquerque, NM, and Livermore, CA ….

Robert E. Mace, Sarah C. Davidson, Edward S. Angle, a., William F. Mullican, I., 2006. Aquifers of the Gulf Coast of Texas, Texas Water Development Board Report 365. Texas Water Development Board, p. 304.

Saribudak, M., 2010. Geophysical mapping of Hockley fault in NW Houston: A few surprising results. Houston Geological Society Bulletin 54, 43-57.

Saribudak, M., 2012. 2D Resistivity Imaging Investigation of Long Point, Katy-Hockley, Tomball, and Pearland Faults, Houston, Texas. Houston Geological Society Bulletin 54, 39-48.

Saribudak, M., Ruder, M., Van Nieuwenhuise, B., 2018. Hockley Fault revisited: More geophysical data and new evidence on the fault location, Houston, TexasGeophysics of the Hockley Fault, Texas. Geophysics 83, B133-B142.

Schmidt, D.A., Bürgmann, R., 2003. Time-dependent land uplift and subsidence in the Santa Clara valley, California, from a large interferometric synthetic aperture radar data set. Journal of Geophysical Research: Solid Earth 108.

Texas, R.c.o., 2021. Texas gas storage operations.

Texas, T.R.C.o., 2022. Online Research Queries, Austin, Texas.

Tolunay-Wong Engineers, I., 2014. Surface fault exploration project: The woodlands, TX. Tolunay-Wong Engineers, Inc. Project No.: 13.13.132, The woodlands, TX.

USGS, 2022. National Water Information System. USGS.

Wang, G., Soler, T., 2013. Using OPUS for measuring vertical displacements in Houston, Texas. Journal of Surveying Engineering 139, 126-134.

Wang, G., Turco, M., Soler, T., Kearns, T.J., Welch, J., 2017. Comparisons of OPUS and PPP solutions for subsidence monitoring in the greater Houston area. Journal of Surveying Engineering 143, 05017005.

Wang, G., Welch, J., Kearns, T., Yang, L., Serna Jr, J., 2015. Introduction to GPS geodetic infrastructure for land subsidence monitoring in Houston, Texas, USA. Proceedings of the International Association of Hydrological Sciences 372, 297-303.

Wang, G., Yu, J., Kearns, T.J., Ortega, J., 2014. Assessing the accuracy of long-term subsidence derived from borehole extensometer data using GPS observations: Case study in Houston, Texas. Journal of surveying engineering 140, 05014001.

Wang, G., Yu, J., Ortega, J., Saenz, G., Burrough, T., Neill, R., 2013. A stable reference frame for the study of ground deformation in the Houston metropolitan area, Texas. Journal of Geodetic Science 3, 188-202.

Wright, T., Parsons, B., Fielding, E., 2001. Measurement of interseismic strain accumulation across the North Anatolian Fault by satellite radar interferometry. Geophysical Research Letters 28, 2117-2120.

Wright, T.J., Parsons, B., England, P.C., Fielding, E.J., 2004. InSAR observations of low slip rates on the major faults of western Tibet. Science 305, 236-239.

Yu, J., Wang, G., Kearns, T.J., Yang, L., 2014. Is there deep-seated subsidence in the Houston-Galveston area? International Journal of Geophysics 2014.

Zebker, H.A., Villasenor, J., 1992. Decorrelation in interferometric radar echoes. IEEE Transactions on geoscience and remote sensing 30, 950-959.

Zhou X., Wang G., Wang K., Liu H., Lyu H., and Turco M. J., 2021. Rates of Natural Subsidence and Submergence Along the Texas Coast Derived from GPS and Tide Gauge Measurements (1904-2020). Surv. Eng. 147 (4): 04021020.